Escola d'Enginyeria de Telecomunicació i Aeroespacial de Castelldefels
UNIVERSITAT POLITÈCNICA DE CATALUNYA

MASTER THESIS

TITLE: Tools for design of satellite constellations for meteor detection and reentry observation

MASTER DEGREE: Master's degree in Aerospace Science and Technology

AUTHOR: Juan Francisco Bertona

DIRECTOR: Andreas Stock

DATE: December, 13th 2018

Title : Tools for design of satellite constellations for meteor detection and reentry observation

Authors: Juan Francisco Bertona

Advisors: Andreas Stock
Garima Pandey

Supervisor: Josep Ignasi Rojas

Date: December, 13th 2018

Overview

The following thesis presents the necessity and advantages of using a constellation of satellites for the observation of meteors, and of spacecraft and debris reentry.
For the purposes of evaluating the performance of such constellations, and as a support tool for the feasibility study and design phases, a suite of analysis algorithms was developed.
For verification, the algorithms are compared to the results of an ealier study on the subject, and to theoretical models where possible. These comparisons include error in meteor mass generation, coverage area and meteor detection rates as a function of altitude and tilt angle of an orbital observatory. In the comparisons, the performance of the algorithms is consistent with the results of the earlier study, and even better in some respects.
In addition, a tentative genetic algorithm optimization scheme is presented.
Finally, in order to illustrate the use of the developed tools in conjunction, two use cases are presented. One, a meteor detection constellation composed of two satellites on the same Sun synchronous orbit, which seeks to maximize double detections. The other, a 3-plane Walker delta constellation optimized to observe the trajectory of a launch vehicle during launch and reentry. Both examples result in sensible constellation configurations, even though the latter is shown not to be the optimum.
The performance evaluation algorithms show to be valid tools for mission design, whereas the optimization scheme will require further studies to demonstrate its usefulness.

Título: Herramientas para el diseño de constelaciones de satélites para deteccion de meteoros y observación de reentradas atmosféricas

Autores: Juan Francisco Bertona

Directores: Andreas Stock
Garima Pandey

Supervisor: Josep Ignasi Rojas

Fecha: 13 de diciembre de 2018

Resumen

En la siguiente tesis se presentan la necesidad y las ventajas de usar una constelación de satélites para la observación de meteoros y reentrada de naves y basura espaciales.
Con el fin de evaluar el rendimiento de estas constelaciones, y de facilitar las fases de estudio de factibilidad y diseño, se desarrolló un conjunto de algoritmos de análisis.
A modo de verificación, estos algoritmos se comparan con los resultados de un trabajo previo sobre el tema, y con modelos teóricos donde es posible. Estas comparaciones incluyen error en la generación de masa de meteoros, área de cobertura y tasa de detección de meteoros como función de la altura y el ángulo de actitud de un observatorio orbital. Las comparaciones muestran que los algoritmos funcionan de manera similar a aquella demostrada en el trabajo previo, e incluso mejor en algunos aspectos.
Además, se presenta un esquema de optimización de algoritmo genético.
Por último, con el fin de ilustrar el uso de las herramientas desarrolladas en conjunto, se presentan dos casos de uso. El primero, una constelación para la detección de meteoros compuesta por dos satélites en la misma órbita heliosíncrona, que busca maximizar la cantidad de detecciones simultáneas. El segundo, una constelación tipo Walker delta de 3 planos optimizada para observar la trayectoria de un vehículo de lanzamiento durante su ascenso y reentrada. Ambos ejemplos resultan en configuraciones de constelación sensatas, aunque se determina que la del segundo caso no es la óptima.
Los algoritmos de evaluación de rendimiento muestran ser herramientas válidas para el diseño de misiones, mientras que el esquema de optimización requerirá más estudios a fin de demostrar su utilidad.

“The ships hung in the sky
in much the same way that bricks don’t.”

CONTENTS

LIST OF FIGURES

LIST OF TABLES

CHAPTER 1. INTRODUCTION

The main motivation for the design of a satellite constellation in this work is to be able to detect and measure the properties of objects flying in the low Earth orbit region and reentering the Earth's atmosphere. Two study cases were identified:

- Meteors
- Debris and vehicle flight and reentry

The characteristics of these phenomena are described in the following section.

1.1. Meteors

1.1.1. Meteoroids, meteors and meteorites

Since in popular culture the terms meteoroid, meteor, and meteorite are frequently confused since they describe different aspects of the same phenomenon it is important to state the difference between them.

Meteoroids

Meteoroids are small interplanetary solid bodies of metallic or rocky composition with masses usually lower than that to be considered an asteroid or a comet. They are usually created from the disintegration of one of such bodies.

Their size (equivalent spherical diameter) ranges from 10 μm upwards, below which the particles are considered space dust. Even though there is no upper bound for their size, a diameter of 10 m is considered a standard bound since these are the largest meteoroids recorded by scientific instruments.

Figure 1.1 shows the ranges of size and mass where meteors are amongst other bodies of the universe.

The luminous phenomenon created at the entry of a meteoroid in the Earth's atmosphere is called a **meteor**.

Meteors

Popularly known as shooting stars, until the early 20th century they were thought to be an atmospheric event rather than one coming from outer space.

Meteors can come from the encounter of the Earth with a stream of meteoroids, usually related to comets, in which case they can form a meteor shower. Those that do not belong to such streams are denominated sporadic meteors, usually related to asteroid disintegration. Usually their duration ranges from a fraction of a second to some seconds, with 10 s being a higher bound.

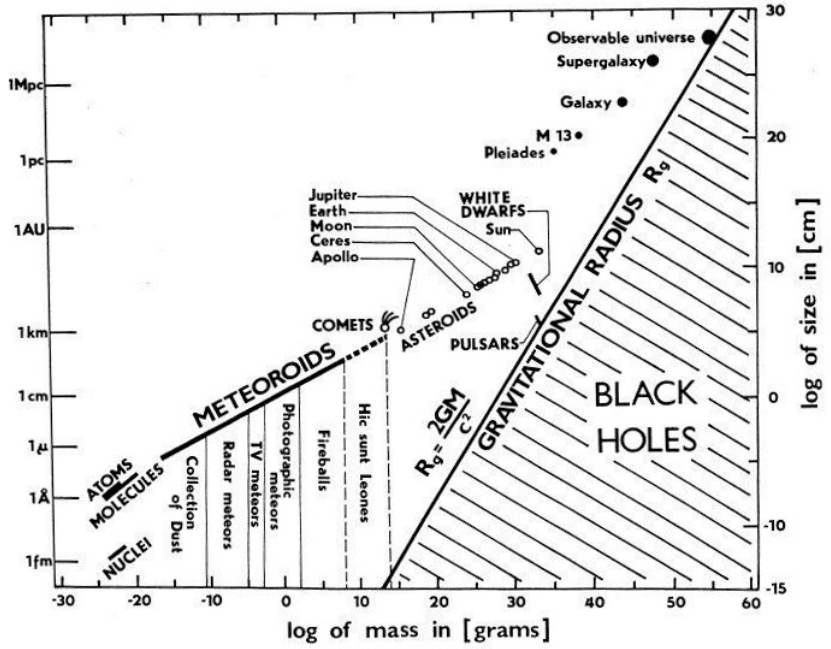

Figure 1.1: Size in function of mass for extraplanetary bodies [1].

Specific kinds of meteors

- Fireball

  This is a type of meteor event with a high brightness, many times resulting in a meteorite. Even though the literature disagrees on the specific limits, a common definition is that a fireball is an event with a magnitude brighter than between -4 and -8.

- Bolide

  A bolide is a type of fireball that fragmentates during the ablation part of the flight.

- Meteor flare

  It is a sudden increase in meteor brightness by at least one magnitude. It is more common in high velocity meteors and is usually caused by a sudden fragmentation or a sudden change in the physical properties of the meteoroid.

Meteorite

In case some mass remains after the meteor and reaches the surface of the Earth, this mass is denominated a **meteorite**. This term should only be used for meteoric bodies recovered from the surface of the Earth.

1.1.2. Other related phenomena

- Meteor wake

  It is electromagnetic radiation emitted behind the meteoroid in contrast to that emitted from the meteoroid, usually called head radiation. The length of the wake is usually of several meters to hundreds of meters and its duration is around some tenths of a seconds after the pass of the meteoroid. Its emission spectra shows lines of the same elements as the head radiation.

- Meteor train

  It is radiation emitted behind the body for seconds or more usually coming from the forbidden lines of neutral or ionized oxygen atoms. Occasionally such trains may last for hours.

1.1.3. Meteor phases

The meteor phenomenon can be divided in four different stages (fig. 1.2):

- Preheating

  As a meteoroid approaches the upper Earth atmosphere (300 - 100 km) its surface starts rapidly heating from the collisions with the constituting atoms of the air. The meteoroid's surface reaches temperatures ranging from 500 K to 900 K depending on its composition.

  When the surface tension (tangential compression) reaches the strength of the material, spallation starts where the meteoroid can start fragmenting. The inside of most meteoroids (except very small grains) remains practically unheated.

- Ablation

  As the meteoroid encounters denser atmospheric gasses the heating is such that its surface reaches 2500 K and it starts ablating material. After reaching this temperature, further increase is then small because most of the kinetic energy is spent in the ablation (including fragmentation) process itself. Given such high temperatures the meteoroid starts emitting electromagnetic radiation, including visible light.

  If 3 km/s is reached somewhere high above the surface and there still remains a significant amount of mass, this mass continues to move without emitting light in a dark flight: there are not enough hot gases around the body any more to emit visible light.

- Dark Flight

  Ablation ceases during this part of the trajectory. There is not enough kinetic energy to either evaporate, or to provide heating. The process is now just the opposite: it is a quick cooling (exponential with time). The trajectory of the object is dictated by the winds it encounters during its flight.

- Impact

  Impact velocities are usually between 10 and 100 m/s for meteorites with terminal mass of 10 g to 10 kg. They usually leave a crater on the ground slightly bigger than the meteorite itself. The trajectory of the impact is hardly related to the pre-ablation trajectory as previously mentioned. If ablation continues all the way to the surface, meaning that the body hasn't slowed down below hypersonic speed, a much bigger impact crater is formed due to sudden explosive release of the enormous kinetic energy.

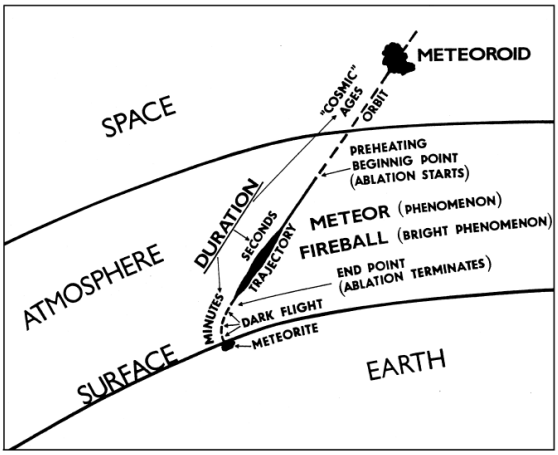

Figure 1.2: Diagram showing the different phases of the colission of a meteoroid with the Earth [1].

1.1.4. Meteor spectra

The electromagnetic radiation emanated from a meteor consists of three different parts. The continuum radiation caused by the meteoroid's high temperature during entry, the ionization of atmospheric gasses, and the radiation emission from the ablated material of the meteoroid in gas form.

The continuum radiation is located mostly in the IR (infrared) spectrum since the temperature of the body is of approximately 2500 K. For the discrete part of the spectrum two different source temperatures can be identified according to [2]. A lower temperature part corresponding to ~4000 K and a high temperature part corresponding to ~10000 K.

The location and intensity of the emission lines indicate the presence and abundance of chemical elements and molecules in the meteoroids. Many of the discrete emission lines are located in the NIR (near infrared) spectrum and in the visible spectrum. Figure 1.3 shows an example.

Unfortunately, some other emission lines such as the Mg II line, which might help better characterize the temperature of the ablation vapor, and the OH and NO, lines which might indicate the presence of prebiotic materials in the meteoroid, are found in the UV (ultraviolet) spectrum and are absorbed by the ozone layer in the atmosphere. The only way to observe such lines is from space.

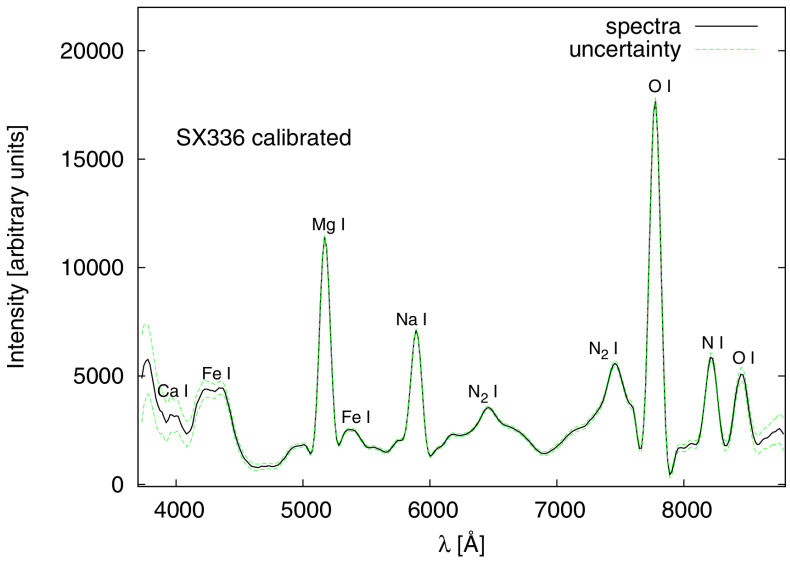

Figure 1.3: Example of the near infrared and visible spectrum of a meteor indicating the discrete emission lines related to specific chemical elements [3].

Figure 1.4 shows an example of a meteor's UV spectrum.

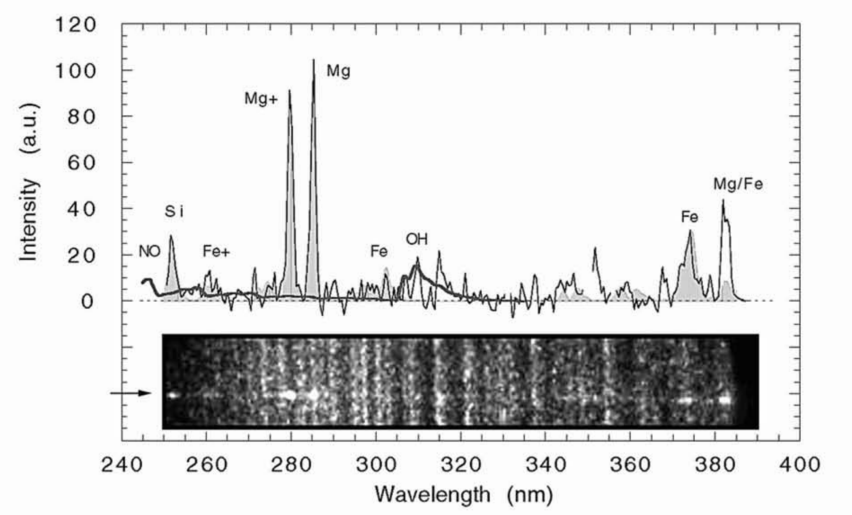

Figure 1.4: One of the UV spectra of meteors obtained by the MSX mission showing the presence of lines that can only be observed in this range of wavelengths such as Mg, OH and NO [4].

1.1.5. Meteor Science

By studying meteoroids and meteorites scientists can better understand topics such as the pre-solar environment, the formation of the Solar system and its evolution as well as the geologic history of the Earth and the Moon.

This is because, since their formation at any of these phases, the composition of most of

them has been unchanged by the processes that later shaped the Sun and the planets. In addition, their trajectories and positions give indications of how mass shifted during the formation of the solar system as well as the events that took place in it.

There is evidence of prebiotic compounds being present in meteoroids [5]. This indicates that such compounds existed before the formation of life on Earth and could give indications on the nature of biogenesis on this planet.

Furthermore, meteor study is a science in itself and, even though it has been an active field of work since the 60's, the prediction of the properties of meteors still relies heavily on empirical laws which vary widely depending on the data which is used to fit them. This motivates the generation of projects that provide more and better measurements of the phenomenon.

1.2. Vehicle reentry

Reentry vehicles are vehicles that are designed to reach the Earth's surface from space. To do so they have to be able to safely withstand the very high temperatures involved in decellerating against the atmosphere at the very high speeds associated with reentry from suborbital or orbital flight.

In contrast to meteors, these phenomena usually take longer times in the order of the tens of minutes, with a higher bound being around 35 minutes, which was the time the shuttle would take from touching the atmosphere until touchdown.

The observation and measurement of such reentries is essential to assess the performance of reentry vehicles as well as to better understand reentry physics.

The sources of radiation that can be observed from these events are the same as the ones from meteors. Namely:

- Blackbody radiation

  From the high temperature of the surface of the spacecraft (up to 2500 K). Also called the continuous component of the emitted spectrum. Mostly in the IR range.

- Shock radiation

  Radiation is emitted from excited electronic states of atoms/molecules of the air that is heated in the shockwave of the incoming spacecraft.

- Ablation products

  All orbital and superorbital reentry vehicles have ablative shields which remove heat from the surface of the spacecraft as it ablates. The materials of such shields emit discrete radiation between the NIR range towards the UV range.

- Chemoluminiscense

  A source of radiation caused by the recombination of O atoms and NO molecules produced in the shockwave. It has been established that a spacecraft travelling faster than the speed of sound leaves NO in its wake. The O attaches to NO and becomes NO_2. About one out of 5 attachments leads to visible light generating a

persistent train that can last for tens of minutes in the sky. It was an unexpected sight behind the space shuttle, first documented by NASA photografer P.D. Maley [6].

1.3. Space debris

Space debris, colloquially called space junk, is the name given to masses of artificial origin orbiting around Earth, mostly comprised of dead satellites, expendable parts of launchers and pieces resulting from their erosion or disintegration caused by collisions.

It is estimated that more than 170 million debris smaller than 1 cm (0.4 in), about 670,000 debris 1–10 cm, and around 29,000 larger debris are in orbit around the Earth [7].

These masses pose a threat to orbiting spacecraft so the understanding of the phenomenon, as well as mitigation strategies, are vital to the continuity and sustainability of space activities.

Figure 1.5 shows damage produced by a piece of space debris or meteoroid to a radiator of the space shuttle.

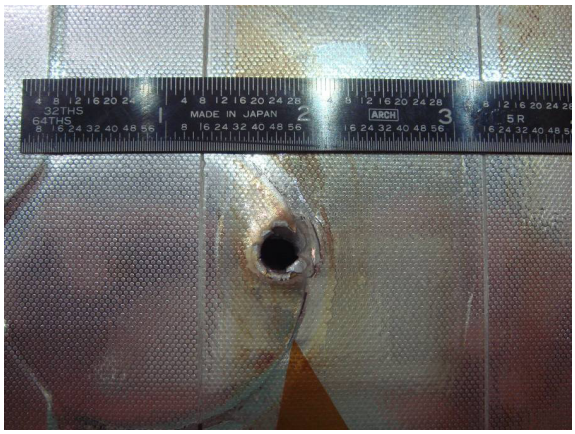

Figure 1.5: Damage done by a piece of space debris on the radiator of a space shuttle [8].

Phenomenologically, the reentry of these bodies to the atmosphere is similar to both, meteors and reentry vehicles depending on the size of the body. Smaller bodies produce a short and faint burst of light similarly to meteors (fraction of a second), while full expendable spacecraft produce longer emissions more similar to reentry vehicles.

Contrary to meteor science, there is currently very little information to produce models that can predict the characteristics of the radiation produced by these events. Therefore, this work focuses on tracking of objects more than detection of these events.

1.4. Observation campaigns

Several observation campaigns have been performed successfully to record spacecraft and debris entry events in order to asses the performance of the spacecraft and better understand debris reentry. The space shuttle, stardust, genesis and hayabusa capsules reentry are some notable examples of succesful vehicle reentry observation. Examples of observation campaigns for space debris include the reentry of a Cygnus cargo spacecraft and the reentry of an unknown object called WT1190F [9].

Figures 1.6 and 1.7 show examples of the results from these kind of campaigns.

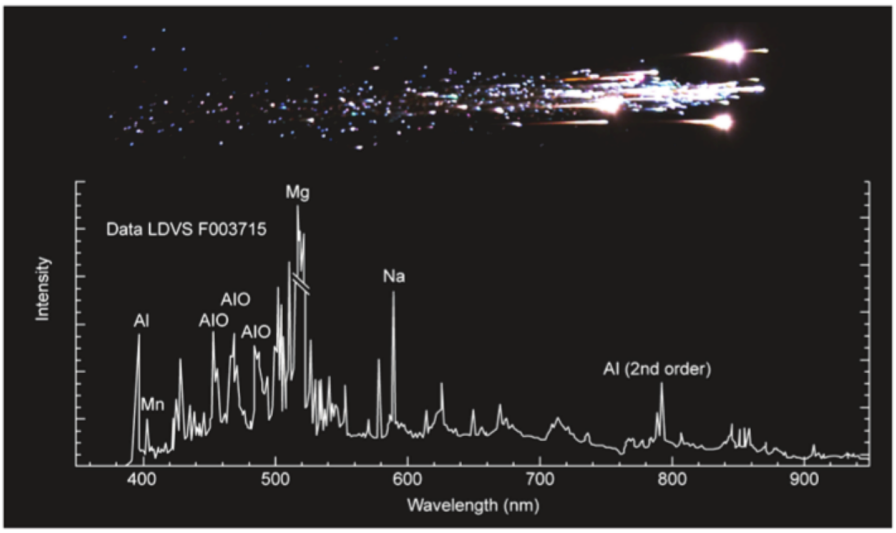

Figure 1.6: Hayabusa capsule spacecraft bus disintegrating during reentry [10].

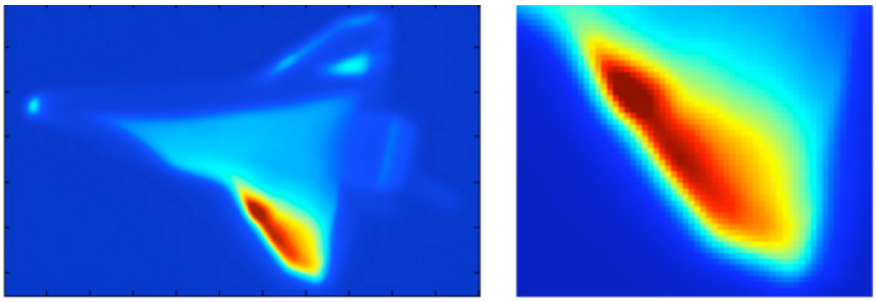

Figure 1.7: Thermal imaging of the Endeavour space shuttle during reentry [11].

All these measurements were performed either from land, from sea or from airplanes resulting in limited access to the UV range and the risk of having the campaign spoiled by bad weather. In order to avoid these problems and improve the science obtained, the use of a satellite constellation as orbital observatory is proposed in this thesis. The reasons behind this are explored in chapter 2.

1.5. Satellite constellations

Satellite constellations are groups of more than one satellite that work together in order to achieve a joint objective. Regarding service, this architecture can provide increased coverage area, shorter revisit time, multiple satellite coverage (e.g.: GPS) and satellite cross communication (e.g.: Iridium).

Regarding operations, a mission comprised of several satellites could offer improved reliability and survivability since losing one satellite could mean no degradation, or just degradation of service instead of loss of mission as in single satellite architecture.

The downside of satellite constellations is the increased cost of having multiple satellites and multiple orbital planes, which require additional launches.

With the advent of miniaturized electronics and propulsion systems, mini and nano type satellites, allowing for easier launch of multiple satellites as well as cheaper satellites, are making this type of architecture increasingly attractive.

Walker delta pattern

This is a very popular constellation pattern in which satellites are placed in circular orbits on equally spaced orbital planes with the same inclination and a certain orbit phasing.

Circular orbits allow satellites to communicate using constant signal strength. The use of the same inclination and eccentricity results in each satellite to be affected by perturbations in a similar way so that station keeping to maintain the constellation is minimized thus saving fuel. The orbital phasing is necesary in order to avoid collisions and interference at orbital plane crossings.

The notation for this kind of constellation is **i: t/p/f** where: **i** is the inclination; **t** is the total number of satellites; **p** is the number of equally spaced planes; and **f** is the relative spacing between satellites in adjacent planes. A better description of the algorithm is given in section 4.6.2..

For example, the Galileo Navigation system (fig. 1.8) is a Walker Delta **56°:27/3/1** constellation. This means there are **27** satellites in **3** planes inclined at **56** degrees, spanning the **360** degrees around the equator. The "**1**" defines the phasing between the planes. That is, difference in starting true anomaly for each plane. Table 1.1 shows the phase for different values of **f** for a constellation like Galileo.

f	Phase [°]
0	0
1	13.33
2	26.67

Table 1.1: Phase values for different values of **f** for a constellation like Galileo.

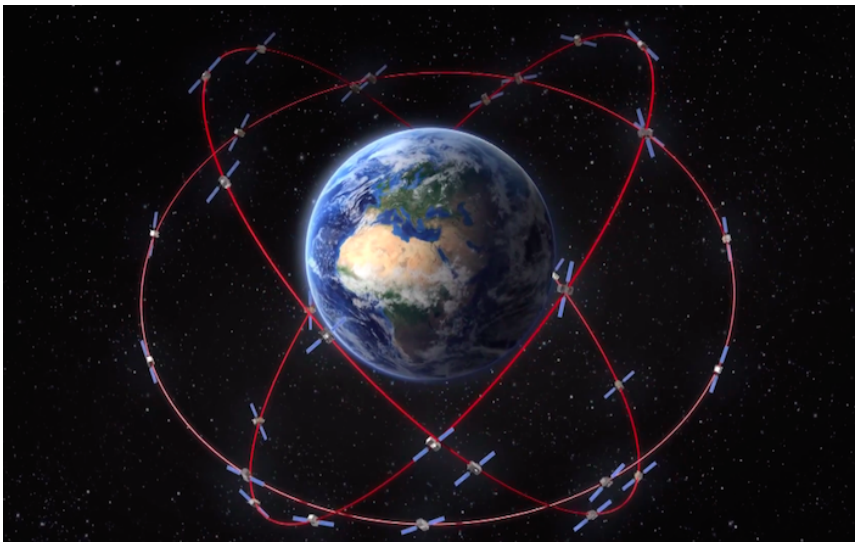

Figure 1.8: Artist impression of the Galileo constellation showing the three orbital planes [12].

Walker star or symmetric polar

This configuration is similar to a Walker Delta but the inclination is close to 90^o (polar orbits) and the orbital planes are equally distributed in 180^o. This last characteristic results in satellites on one side of the Earth traveling North and the ones on the other side traveling South.

An example of this kind of constellation is the Iridium communication network which has a **86.4^o:66/6/2** Walker Star configuration. Meaning it consists on **66** satellites on **6** different planes with an inclination of **86.4^o**.

Other constellation configurations

These are only two examples of constellation design patterns. Some other popular ones are for example: “Streets of Coverage” or “Non polar Perpedicular Planes” [13].

All the previously mentioned patterns consist of circular orbits. Some popular patterns with non-circular orbits are, for example, “Molniya”, “Tundra” or “Flower” [14] constellations which might prove useful for certain cases. Non-circular orbits have not been considered for the present work but would be a natural extension to the capabilities of the constellation design tool developed. More information can be found in the provided references.

1.6. Genetic algorithm

In order to find optimal or close to optimal parameters for constellations, the use of a genetic algorithm is proposed and was implemented for this thesis.

A genetic algorithm is a metaheuristic algorithm inspired by the process of natural selection that belongs to the larger class of evolutionary algorithms. It utilizes biologically inspired operations such as selection, crossover and mutation in order to improve the total fitness of a population of solutions and therefore obtain a close to optimal solution.

It is particularly well fitted for problems where the solution space is too large to be completely sampled or the solution topology is not smooth enough. It is one of the latest trends in constellation design and has been successfully used in several optimization cases [15][16][17].

The first step in this kind of algorithm is to randomly generate a population of solutions. Then the fitness of each solution is evaluated. Fitness is the performance of an individual towards a certain goal. It can be, for example, coverage area, revisit time, or, for this work, meteor detection rate.

Then, the individuals with the best fitness are selected and the rest are removed from the population emulating the "survival of the fittest" rule of Darwin's theory of evolution. The remaining individuals are crossed creating children with characteristics of the two progenitors. Figure 1.9 shows an example of "two point" crossover.

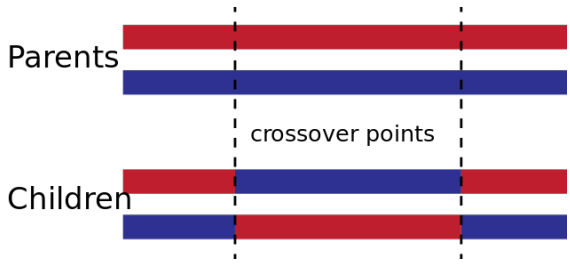

Figure 1.9: Example of crossover of individuals in a genetic algorithm.

Some of the individuals of the population are mutated, randomly changing one or more of their attributes. This operation inserts new information into the system. Finally, the fitness of all the new individuals is evaluated and the process starts again.

Each new population is called a "generation". The algorithm is usually run for a fixed amount of generations or until an objective fitness is reached, saving at each generation the fittest individuals of all time. The evolution can be easily resumed from the last generation.

Due to the fitness evaluation of each individual being independent, these algorithms are easily parallelized to reduce computational time.

CHAPTER 2. MOTIVATION

2.1. Orbital observatory

The benefits of having the observation instruments for these phenomena mounted on an orbiting spacecraft would be the following:

- Independence from meteorological effects

  These phenomena take place in the higher part of the atmosphere, above from most meteorological effects.

- Higher coverage area

  The higher possible distance from the phenomena as well as the absence of the horizon would allow to increase the covered area and therefore the amount of observed events.

- Access to the UV spectrum

  Due to the presence of the ozone layer it is not possible to observe the UV characteristics of the phenomena from the ground.

- Negligible atmospheric attenuation

  As the atmosphere is less dense in its higher parts, the attenuation of signal with distance would be lower than from a terrestrial observatory.

In addition, by using a constellation of satellites instead of a single spacecraft:

- Stereoscopic measurements of events can be performed in order to be able to determine the position and velocity of entering bodies.

- Visibility in time can be ensured or improved for the case of longer phenomena such as vehicle reentries.

2.2. Past and current missions

2.2.1. Midcourse Space Experiment (MSX)

The MSX satellite was funded and managed by BMDO (Ballistic Missile Defense Organization, currently Missile Defense Agency or MDA) with JHU/APL (Johns Hopkins University/Applied Physics Laboratory) as the prime contractor, spacecraft integrator, and operator of the mission. It served as a first system demonstration in space of technology to identify and track ballistic missiles during their midcourse flight phase, hence its name. Its suite of optical sensors cover the spectrum from the far ultraviolet (110 nm) through the very-long-wave infrared (28 μm) spectrum [18].

Using data from the experiment, the first UV spectrometries of meteors were performed.The new data provided the first spectral confirmation of the presence of molecular OH and NO emission in meteor spectra, which are prebiotic compounds [4].

It was decomissioned in 2008 after 12 years of successful operation.

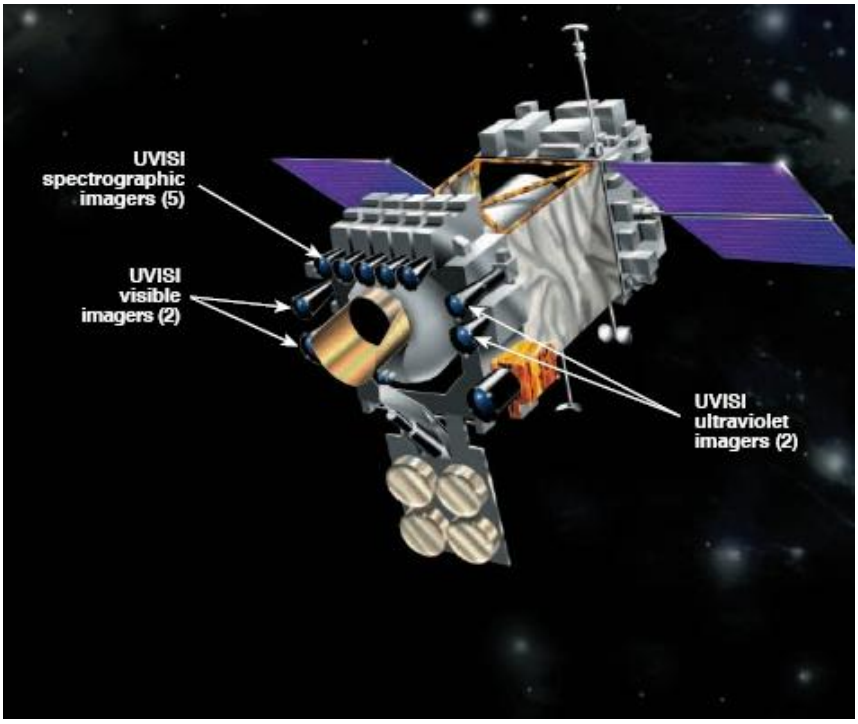

Figure 2.1: Drawing of the MSX satellite indicating the position of the UV detectors [18].

2.2.2. Space Based InfraRed Sensor (SBIRS)

After the technology demonstration of MSX, the SBIRS project was started, managed by the MDA. It consists of a network of satellites in geostationary and highly elliptical orbit also with the purpose of tracking ballistic missiles as well as their decoys during the midcourse phase. An extra layer in low Earth orbit is currently being planned.

Its instrument consists of a “scanner” IR sensor with a wide field of view (FOV) and a “starer” sensor with a narrower FOV to aim at the target once it has been identified.

The project has proven to be very costly at a price of over 900 million dollar each satellite for the GEO version.

With the data obtained from the IR sensors one of the most important studies on bollide flux and luminous efficiency was produced [19].

2.2.3. Chitech Observatory of METeors on iSS (COMETSS)

As its name indicates, this observatory was a HDTV camera mounted on ISS. Its objective was to perform spectral analysis of the main components of meteors by using spectrom-

etry[1] of the radiation emitted in the visible spectrum. The targets were be high zenithal hourly rate meteor showers such as the Perseids or the Geminids [20].

The experiment took place between March 2016 and August 2018 and its results are yet to be published. One of the obtained pictures can be observed in figure 2.2.

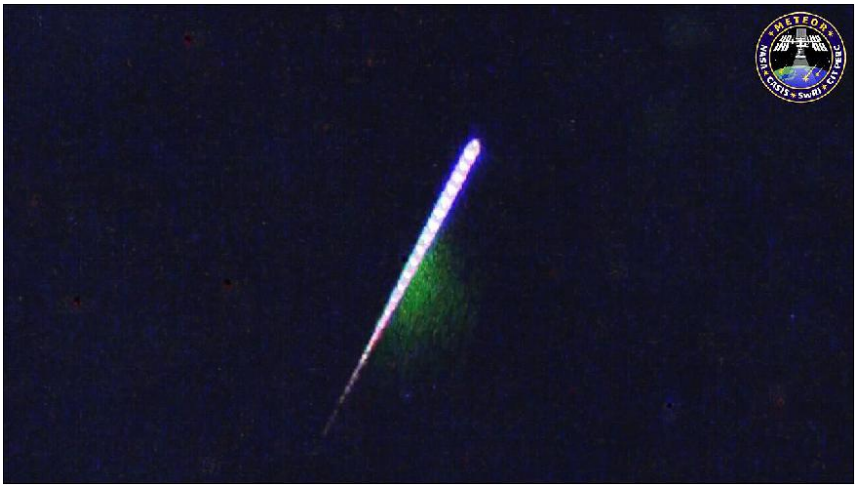

Figure 2.2: Meteor captured by the COMETSS camera from the ISS [21].

2.3. Proposed missions

METEORIX

METEORIX is a pedagogic project initiated in 2013 by the Université Pierre et Marie Curie (UPMC, Paris) and the Institute of Celestial Mechanics and Ephemeris Calculations (IMCCE - Paris Observatory) as part of the JANUS projects. It is supported by various collaborations with several institutes such as the Laboratoire d'Informatique de Paris (LIP6), the Laboratoire Atmosphères, Milieux et Observations Spatiales (LATMOS) and the French Space Agency - Centre Nationale d'Etudes Spatiales (CNES). It is intended to complement the Fireball Recovery and InterPlanetary Observation Network (FRIPON) [22].

The objective of the project is to design, build and launch a 3U cubesat that can detect and characterize meteors from orbit. Even though the initial design was supposed to house a UV spectrometer, due to volume and mass restrictions the project evolved to an only visible detector. Figure 2.3 shows the preiliminary design of the METEORIX satellite.

[1] Spectrometry is a technique by which the intensity of electromagnetic radiation is measured as a function of frequency or wavelength.

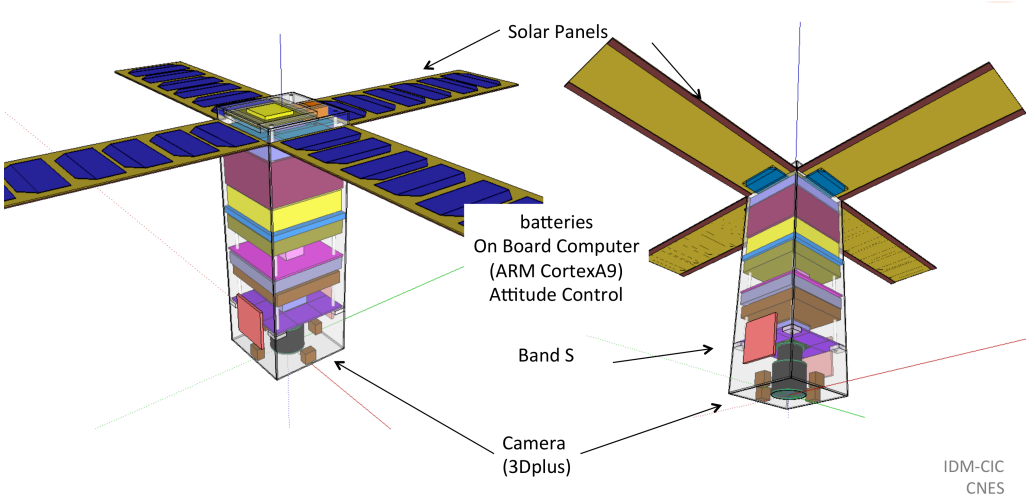

Figure 2.3: Preliminary design of the METEORIX 3U cubesat [23].

2.4. Summary

By studying the previous and current existing missions the following shortcomings were identified:

- Most information not publicly available since most projects are of military nature
- Very expensive platforms and instruments
- No UV spectrometry at the moment, resulting in insufficient composition characterization
- No object tracking through stereo imaging

Given the advantages of using a constellation of satellites in order to observe meteor, debris and vehicle entries to the atmosphere, and the shortcomings of the existing orbital observation missions, it becomes evident that a scientific mission with these characteristics is necessary for further advances in the area. This thesis develops tools that can aid in the design and feasibility studies for such mission.

CHAPTER 3. OBJECTIVES AND REQUIREMENTS

3.1. Meteor detection and tracking

Part of the objectives of the present thesis was to investigate and lay down mission objectives and requirements that would be appropriate for a cheap constellation of small satellites with the capabilities to track meteors and/or other reentering objects. As a guide for future mission designs and as a synthesis of the information previously presented, the resulting mission objectives and requirements are presented in tables 3.1.1. and 3.1.2. for meteor detection and tables 3.2.1. and 3.2.2. for vehicle and debris reentry tracking.

3.1.1. Objectives

Objective	Motivation
Detect and measure meteors from orbit	Meteor science relies heavily on experimental data. An instrument in orbit would find intself in a vantage point where it could easily cover more surface than a land based one. In addition, from outer space, signal attenuation produced by the atmosphere is negligible, particularly in the UV range where almost no information can be obtained from the ground.
Measure trajectory and velocity of meteors	This information can be used to determine the meteoroids original orbit to determine their origin. Additionally, to better characterize the flux of meteoroids into the atmosphere.
Produce UV spectroscopy of meteors	The hot component of a meteor's light is produced by the hot vapor resulting from the ablation of its material. By analizing the UV component of the meteor's radiation, its composition can be better determined. The composition of a meteor is important since it reflects the composition of the solar system when it was formed and might even shed clues into the formation of life on Earth.

Table 3.1: Objectives for a meteor detection satellite constellation.

3.1.2. Requirements

Mission requirements	**Motivation**
The constellation must detect and measure the highest possible amount of meteors with the least amount of orbital planes and satellites on each plane.	Each orbital plane means a different launch or expensive maneuvers for each satellite increasing the cost. Each extra element in the constellation increases the cost of the mission.
The satellites must use “commercial off the shelf components” (COTS) where available.	COTS components are those that have a high technology readiness level (technology demonstration, validation and if possible flight heritage) and can be easily obtained in the market, meaning that they do not have to be specifically designed for the mission, are probably mass produced, and have no, or very few, purchase restrictions. They are therefore cheaper and more readily available, resulting in a cheaper and faster deployment of the mission.
The highest proportion of detected meteors have to be detected by 2 or more of the satellites.	Trajectory can not be determined using a single measurement.
The satellites must have IR-Visible cameras.	Most of the radiated energy from a meteor is emitted in the continuum spectrum in the IR range. The background of the Earth might be a problem regarding signal to noise ratio, even during night, so visible spectrum cameras might be preferred.
Satellites must have UV spectrometers.	To produce UV spectrometry.

Table 3.2: Requirements for a meteor detection satellite constellation.

3.2. Object reentry tracking

3.2.1. Objectives

Mission objective
Detect objects of interest within a series of proposed parabolic or reentry trajectories.
Once an object has been detected, obtain its position and velocity for the longest duration possible.

Table 3.3: Objectives for an object reentry tracking satellite constellation.

3.2.2. Requirements

Mission requirements	**Motivation**
The constellation must cover a specific region of space and the atmosphere where object trajectories might happen.	
The satellites must have IR cameras with a sufficient FOV in order to cover the region of interest most of the time.	IR spectrum is the typical way of finding spacecraft since they are either hot from the launch, have thermal control systems or heat up during reentry.
Once detected, at least two satellites must have the object within visibility.	In order to determine trajectory.

Table 3.4: Requirements for an object reentry tracking satellite constellation.

CHAPTER 4. TOOL DEVELOPMENT

Two main programs were developed. One with the objective of quantifying the performance of a satellite constellation for tracking reentry vehicles and long debris reentries. The other one to assess the performance of a constellation for meteor detection, taking into account the latest meteor physics models and obtaining as a result the simple and multiple hourly detection rates.

In addition, two complimentary programs were developed. One to calculate instantaneous and averaged coverage area from the satellites to a sphere above the Earth. The other, to calculate coverage volume from the satellites to a volume around the Earth.

Finally, a simple genetic algorithm optimization scheme was implemented in order to obtain the best detection or tracking solutions while minimizing amount of satellites.

4.1. Tracking

The Tracking Analysis Tool (TAT) is a tool that takes as input the track of an object in space with Cartesian coordinates as well as the characteristics of a constellation to observe it. The output is an assessment of how well the constellation tracks the event by showing how many satellites observe the object in average at each moment in time taking into account different initial configurations.

4.1.1. Input

Track

This program takes the track as input through a ssv(space separated) file with the following format (header optional):

```
#          t            x            y            z
#        [s]         [km]         [km]         [km]

        0.000     5001.882     1529.229     3637.867
        1.000     5001.886     1529.230     3637.870
        ...       ...          ...          ...
        1532.000  3463.154    -1717.922     5055.954
```

where t is given in 1 s increments and the spatial coordinates are given in Earth Centered Earth Fixed (ECEF) reference system. They can also be given in the Earth Centered Inertial (ECI) reference frame.

Constellation configuration

The constellation configuration file is passed through a json file containing a dictionary as the following example:

```
{
        "constellation":
        [       {
            "kind": "p",
            "altitude": 500,
            "sat_per_plane": 5,
            "inclination": 10,
            "fov": 175,
            "azimuth": 180,
            "elevation": 0,
            "raan_offset": -90
                }
        ]
}
```

More detail on the constellation configuration options can be found in section 4.6..

4.1.2. Main algorithm

A satellite constellation is built from the configuration file provided.

Then, the case is run a chosen amount of times for the complete track. In each iteration a random moment in the sidereal day is chosen for the initial position in ECI coordinates as well as a random moment in the constellation's orbit. For each time step, visibility from each satellite is analyzed and saved and then the orbital positions are propagated one step forward.

Once the case is analyzed for all the required iterations the "time vs satellites with visibility" curves for every case are averaged. This curve is output to a file and a graph is generated for it.

Figure 4.1 shows a flowchart of the main program.

The program has an option that outputs a video for one particular starting configuration, showing the positions of the satellites as well as the tracked object and connects red lines when the object is within visibility. In addition, the time vs visibility graph for this case is created.

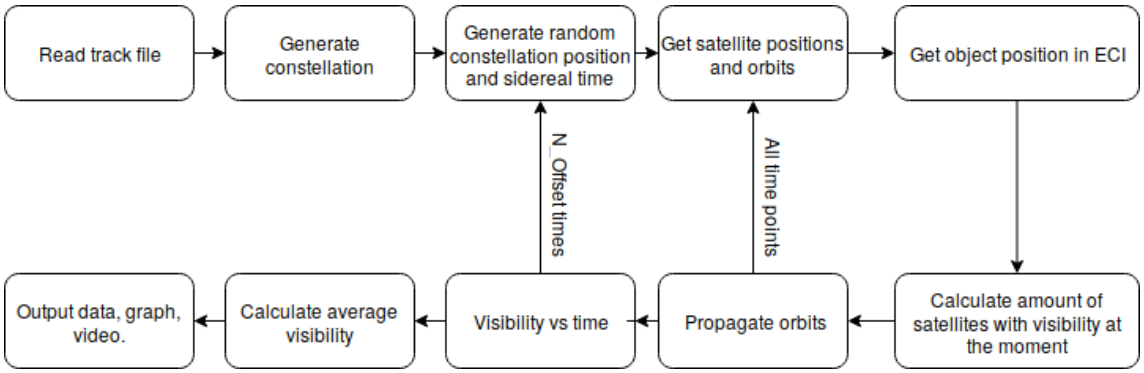

Figure 4.1: Flow chart of Tracking Analysis Tool (TAT) main program.

4.2. Meteor detection

This tool takes as input a constellation and analyzes its average hourly meteor detection rate as well as the meteor tracking rate, that is, meteors detected by two or more satellites simultaneously.

The starting point for this program is a paper called “Simulation of the capabilites of an orbiter for monitoring the entry of interplanetary matter into the terrestrial atmosphere” by Bouquet et al. [24] where the program “Simulator for wide area recording of meteors from space” (SWARMS) is presented. Having as motivation the same reasons explained in the present work, it seeks to study the possible hourly detection rates of an orbiter imaging meteors as well as its dependence with orbit altitude and tilt angle.

In order to properly simulate meteors, it compares and reviews available literature, models and experimental data regarding mass, velocity and density distributions. It also obtains new functional dependencies for derived parameters so, at the end, the amount of light produced by each generated meteor can be calculated. Taking this into account and the optical properties of the detector, the meteor can then be counted as detected or not.

Most of the property distributions found in the Bouquet et al. paper, are the ones used for the present work. The Meteor Constellation Analysis Tool (MCAT) developed for this thesis and here described, can be considered an extension to the tools developed for the Bouquet et al. paper.

More information on the meteor property distributions, the differences between the proposed approach and Bouquet et al.’s approach can be found in section 4.2.2.. A comparison of performance can be found in the chapter 5, “Verifications”.

4.2.1. Main algorithm

The tool first generates the satellite constellation from a json configuration file as described in section 4.1.1.. Then, the meteor positions are randomly generated on the night side semisphere of the Earth at an altitude of 100 km. From the positions of the meteors and the satellites, as well as their FOV cones, visibility is determined for each satellite.

The meteor events within visibility are randomly assigned basic properties (mass, velocity

and density) and then their derived properties (ablation coefficient, luminous efficiency, kinetic energy) are calculated. The apparent magnitude of the events for each satellite are calculated with the distance from each satellite to each event. The apparent magnitude of the event is compared to the maximum magnitude (least bright) detectable event taking into account the properties of the detector used. This way, detection of each event by each satellite is detemined and single and multiple (more than one satellite detecting the event) detections are accounted for.

Each detection is multiplied by a position dependent weight to account for diurnal variations in meteor flux. Finally, the total amount of detections is multiplied by a normalization factor to obtain the hourly detection rate.

Then, the orbits are propagated and the process is repeated until an orbit has been completed to obtain the average detection rate for an orbit. The position of the meteors are kept for all time steps to reduce computational time.

Figure 4.2 shows a flowchart of the main program.

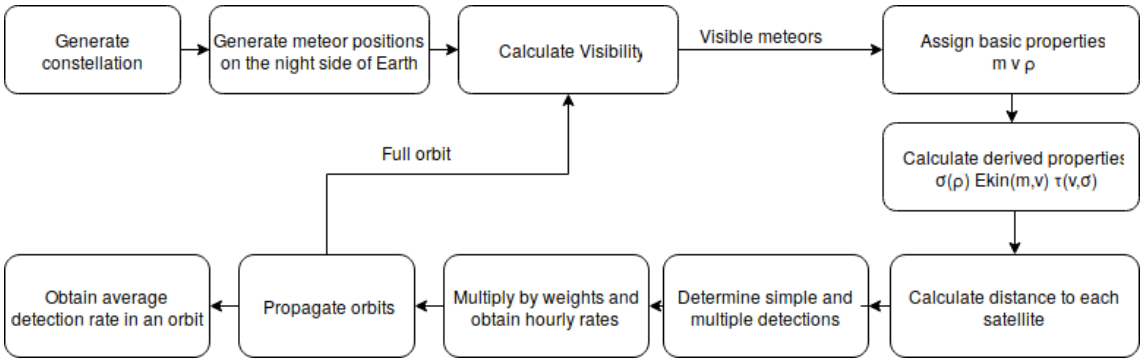

Figure 4.2: Flow chart of MCAT main program.

4.2.2. Meteor Properties

Position

The positions of the meteor events are generated randomly on the surface of a sphere using the Marsaglia [25] method in order to obtain a homogeneous distribution and save computational time compared to the elimination method.

For the case of MCAT, a semisphere is desired for the night side of Earth, so all positive Y coordinate values are replaced by their negative.

The difference with SWARMS is that the approach proposed in the present thesis gives a continuous distribution of positions as opposed to discrete mesh positions. In SWARMS meteors are only generated in a finite amount of positions. The location of these points is the result of a mesh of discrete latitudes and longitudes. This approach results in shorter calculation times for positions but less accuracy when calculating coverage. In MCAT, the positions where meteors are generated are evenly distributed on the night side of Earth.

Mass

The mass distribution used is the one suggested by Halliday et al. [26] shown in formula 4.1.

$$\begin{cases} \log N = -A_1 \log M + B_1 & M < 2.4kg \\ \log N = -A_2 \log M + B_2 & M > 2.4kg \end{cases} \tag{4.1}$$

$$A_1 = 0.48 \qquad B_1 = 3.3$$
$$A_2 = 1.06 \qquad B_2 = 5.26$$

It is a complimentary cumulative distribution function where N is the number of objects with initial mass above M (in grams) per year and million km^2 (fig. 4.3).

In order to sample this distribution, a continuous sampling approach was used in opposition to the discrete sampling used in [24]: A random N is calculated and the value of M is obtained through the inverse of eq. 4.1 and assigned to the meteor.

The masses are generated in the range between 1×10^{-4} g, because objects below this mass cannot be detected optically, and 30 kg, because events with a higher mass are highly improbable (less than $2 \times 10^{-3}\%$ probability). These limits can be changed if the user desires to consider different detection techniques or less probable events.

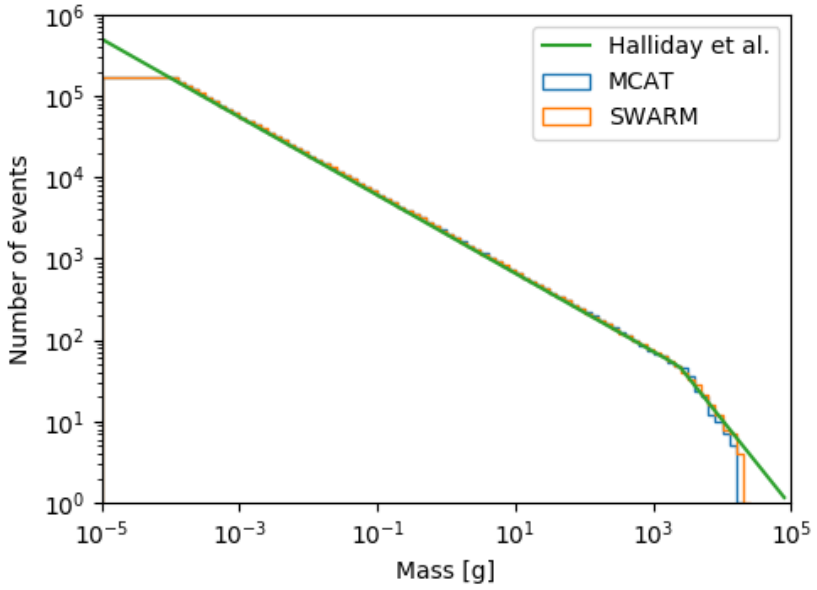

Figure 4.3: Complimentary cumulative mass distribution function suggested by Halliday et al. compared to histograms of the distribution sampled using the SWARM and the MCAT method.

Velocity

The velocity distribution is sampled from a normal probability density function of the logarithm of the velocity reflecting the more frequent occurrence of slow events, as suggested by radar surveys [27].

Meteoroids travel around the Sun in a variety of orbits and at various orbital velocities. The fastest move at about 42.5 km/s through space in the vicinity of Earth's orbit. This corresponds to the Sun's escape velocity or the highest velocity for a body to be bound to the solar system, corresponding to a parabolic orbit. When a collision with the Earth's atmosphere takes place, velocities of meteors result from the movement of Earth around the Sun at about 30 km/s, the orbital speeds of meteoroids, and the gravity well of Earth.

The velocity distribution is therefore truncated at lower and upper limits. The lower one 11.2 km/s (only gravity of the Earth), the upper one 72.8 km/s (42.5 km/s for a parabolic orbit at Earth's perihelion plus 30.3 km/s the velocity of the Earth at perihelion) [1].

Figure 4.4 shows this probability density function sampled using the tool.

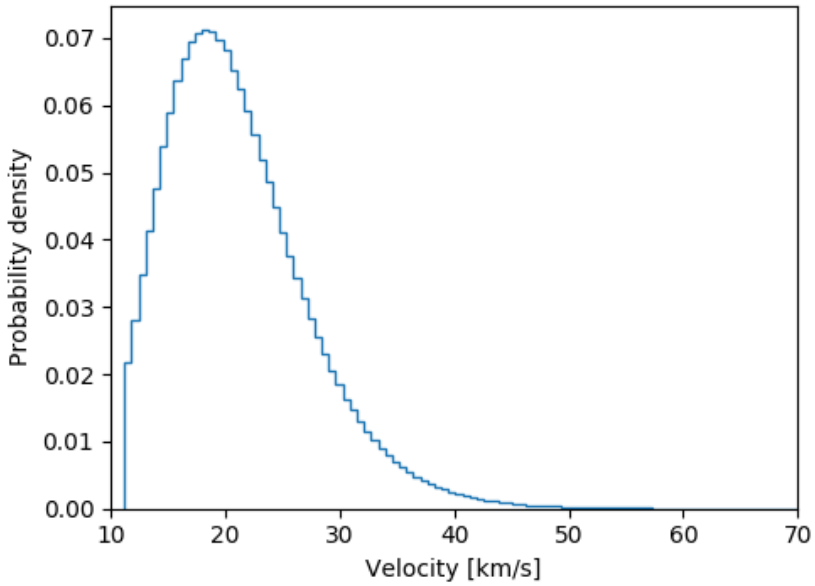

Figure 4.4: Sampling of the velocity probability density function.

Density

The density for meteors is sampled from an homogeneous distribution between 1000 kg/m^3 and 4000 kg/m^3. This is the bulk density indicated by [1].

Ablation coefficient

The ablation coefficient (σ) is a ratio that relates how much a meteor decelerates versus how much mass is ablated per time unit. Most models indicate that it is a function of density.

The formula used comes from an empirical inverse exponential law (eq. 4.2) fitted by [24] from data of the Canadian Network meteor catalog [26].

$$\sigma = -\frac{1}{23.5} \ln \frac{\rho - 0.25}{4.77} \tag{4.2}$$

Luminous efficiency

Luminous efficiency (τ) is a factor that relates kinetic energy loss to luminous energy produced (eq. 4.3). If the whole mass is lost in ablation, as is the case with most meteoroids colliding with Earth, a global luminous efficiency ($\bar{\tau}$) for the whole event can be defined as 4.4.

$$\frac{dE_{lum}}{dt} = -\tau \frac{1}{2} \frac{dm^2}{dt} \tag{4.3}$$

$$dE_{lum} = \bar{\tau} \frac{1}{2} E_{kin} \tag{4.4}$$

In SWARMS, a least square fitting of the data in the Canadian Network meteor catalog was performed to obtain the following empirical law, which relates density and initial velocity with global luminous efficiency.

$$\bar{\tau} = 0.0051(V - V_0)^{0.87}(100\sigma)^{-1.46} \tag{4.5}$$

where V_0 is a reference velocity of 10 km/s.

4.2.3. Detection

The kinetic energy and luminous efficiency are used to calculate the total luminous energy released by a given event. Then, the minimum detectable luminous intensity I_{min} is deduced from the maximum apparent magnitude detectable by the system and the distance from the event to the system. An event is considered to be detectable if its total energy is sufficient to maintain a luminous intensity above I_{min} for the time necessary to appear on a minimum number of frames n_{frames} depending on the instrument used. The total luminous energy necessary to fulfill this condition, assuming a steady emission, is given by:

$$E_{steady} = I_{min} n_{frames} t_{frames} \tag{4.6}$$

with t_{frames} being the duration of exposition for one frame.

The above calculation assumes that the meteor light emission is steady during the event duration, which is not the case. The shape of the light curve has to be taken into account;

it is possible to approximate light curves as a Gaussian function of reduced time. A factor F can be determined to apply on total luminous energy, so that a Gaussian profile of light curve featuring a total energy of $F \times E_{steady}$ would be visible for as long as a constant emission with a total energy of E_{min}. Thus:

$$E_{min} = I_{min} n_{frames} t_{frames} F \tag{4.7}$$

The factor F was found to be 18.51 by analyzing data from the Canadian Network catalog [24].

Depending on the definition of intensity, and thus E_{min}, respect to the event's relative magnitude, varying results are obtained. While most solutions provide results in the same order of magnitude, the same definition (eq. 4.8) as in SWARMS was used for this work in order to be able to benchmark and compare its capabilites.

$$E_{min} = 10^{(3.185 - 0.4 m_{ref})} \left(\frac{d}{d_{ref}} \right) t_{frame} F \tag{4.8}$$

where m_{ref} is the maximum (least bright) apparent magnitude detectable by the instrument and d_{ref} is a distance of 100 km, which is the standard reference distance for magnitudes in meteor science.

4.2.4. Diurnal flux variation

As the Earth translates about its orbit, it encounters more meteoroids and with a higher velocity with its dawn side and less meteoroids with its dusk side. In order to account for these effect a detection weighting scheme was implemented.

From the data presented in [28] a weight function was fitted to obtain weights depending on the position respect to the terminator line (fig. 4.5). The terminator is the line that separates the portion of Earth experiencing daylight from that experiencing darkness, it is perpendicular to the line pointing from Earth towards the Sun. More information on the data fitted can be found in appendix A.

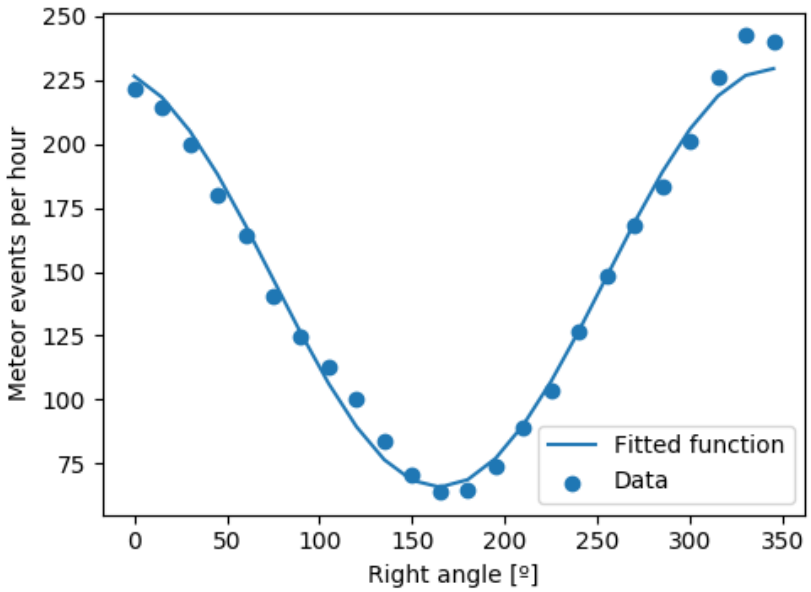

Figure 4.5: Fitting of the weighting function to the diurnal variation in meteoroid flux.

The normalized weight equation obtained is:

$$W = 0.55472903\cos(\theta + 0.26825051) + 1 \tag{4.9}$$

where θ is the angle (in radians) of the projection of the position on the Equatorial plane respect to the dawn line.

Figure 4.6 shows a colour map indicating the weights given to meteors happening on the night side of the Earth.

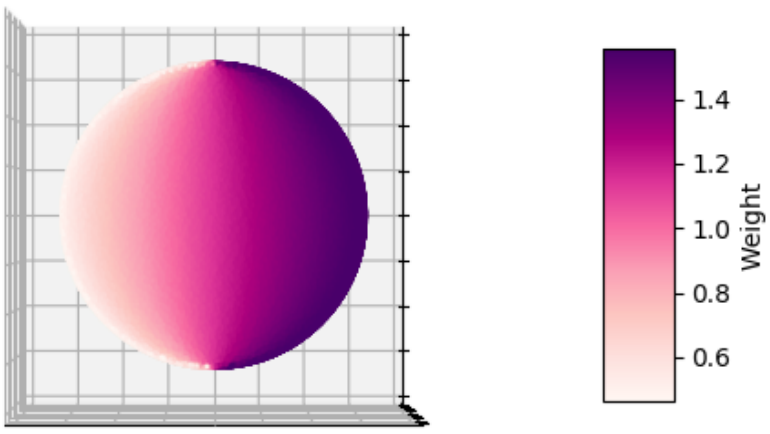

Figure 4.6: Weights on the night side of the Earth.

Each detection is, at the end, multiplied by its weight so that a detection on the dawn side of Earth accounts for more detections than one happening on the dusk side. This will result

in satellites and constellations covering the dawn side performing better than the ones not covering it.

This weight scheme was implemented since there is no readily available information on the diurnal variation in meteor properties (flux, mass, velocity, etc.) to serve as input for the model.

4.2.5. Scaling factor

Each simulation, a fixed amount of meteor position points (N_{points}) are generated on a semispherical surface with area S_{points}. A higher amount of meteor events means more precision in the results but at higher computational cost.

The mass distribution being used is given in total amount of events per million km^2, per year (N_{events}). This value, in the distribution presented in equation 4.1, corresponds to the value of N for the lower bound in meteoroid mass.

To bridge this difference and translate the results of the simulation from detections out of the generated points into hourly detection rate, the following multiplication factor is used on the result:

$$factor = \frac{N_{events}}{N_{points}} \cdot \frac{S_{points}}{24 \cdot 365} \tag{4.10}$$

$$S_{points} = 2\pi(r_{Earth} + alt)^2 1 \times 10^{-6} \tag{4.11}$$

where alt is an altitude above the surface of the earth of 70 km as defined by [26].

4.3. Coverage calculation

An auxiliary algorithm was developed in order to estimate coverage of a constellation. The Monte Carlo (MC) nature of the previous algorithms was exploited for this end. As is typical in examples of MC integration, coverage can be estimated as the proportion of points randomly generated in a surface or a volume which are within vision, leading to solutions which would be very hard or impossible to obtain analytically.

The points for the spherical surface are generated following the Marsaglia method.

Points can be also generated in the volume comprised between two concentric spheres of different radii by using the elimination method. This method randomly generates points in the volume of a cube. If the module of the coordinates is outside the radii interval, it is repicked. This method is not a very efficient one but it is fast enough for the calculations performed. It could be easily replaced by a faster algorithm, should the need arise.

The algorithm can return either an instantaneous coverage value or the average single and multiple fold coverage for a period of the constellation.

Figure 4.7 shows a flow diagram of the algorithm.

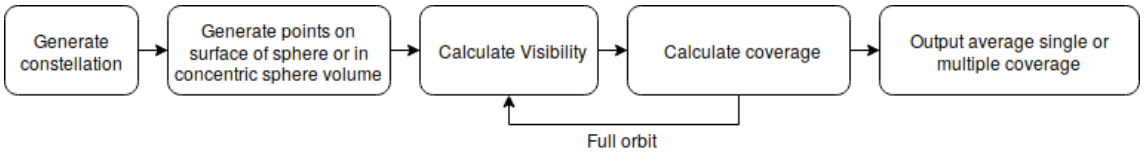

Figure 4.7: Flow chart of the Monte Carlo coverage tool.

4.4. Optimization scheme

An optimization scheme using genetic algorithms was implemented. Far from being the focus of this thesis, it is presented as a proposal for future works and as a means to obtain results to present as examples of use cases of the tools presented.

The framework used for this scheme is Distributed Evolutionary Algorithms in Python (DEAP) which is publicly available in github [29][30]. DEAP is a novel evolutionary computation framework for rapid prototyping and testing of ideas. As its name indicates it is compatible with parallelisation mechanisms such as “multiprocessing” and “SCOOP”.

The algorithm used is a modified version of the `eaSimple` algorithm which reproduces the simplest evolutionary algorithm as presented in [31]. The algorithm was modified so that evolution could be resumed from the last population.

4.4.1. Fitness

Fitness is a measure of how well each solution or individual performs in order to achieve an objective. In order to keep the optimization simple, single objective optimization was used instead of multiobjective.

MCAT

The fitness (Q) of each solution for MCAT was defined as:

$$Q = \frac{Average\ hourly\ multiple\ detection\ rate}{Amount\ of\ satellites} \tag{4.12}$$

This definition gives a higher fitness value for a higher average rate of multiple detections, and a lower value for constellations that use a higher amount of satellites due to the increased cost. This simple relationship implies that a constellation with half the amount of satellites that achieves half the detection rate is just as good as its counterpart.

A more advanced approach to fitness would be to use a function such as:

$$Q = W_1(MDR) - W_2 N_{sats} - W_3 N_{planes} \tag{4.13}$$

Where MDR is the average hourly multiple detection rate, N_{sats} is the amount of satellites and N_{planes} is the amount of planes. W_2 and W_3 are weights related to the cost of each satellite and of each orbital plane. These weights are of course related to mission and satellite design and mission architecture and would be available once there is an initial

mission definition. Finally, W_1 is a weight related to the subjective assignment of how much the science resulting from this mission is worth, or how much the client is willing to pay for a better performing mission.

TAT

The fitness function assigned to tracking analysis is proportional to how long the object is being observed by two or more satellites (object being tracked) compared to the total amount of time where the object is detectable and weighted by the amount of satellites (eq. 4.14).

$$Q = \frac{Time\ object\ being\ tracked}{Total\ detectable\ time \times Amount\ of\ satellites} \tag{4.14}$$

A fitness function in the fashion of eq. 4.13 could also be used.

4.4.2. Selection

Selection is the process where some of the fittest individuals survive in order to pass their genes to the next generation.

The selection algorithm used is of type “Tournament”. This algorithm selects the fittest individual out of a randomly chosen group and repeats the process for the same amount of times as individuals. The size of the group used is 3.

4.4.3. Crossover

Crossover is the process where the selected individuals cross in order to create new individuals that have their genes. The type of crossover used is two point crossover which is ilustrated in figure 1.9. The crossover probability used is 50%.

4.4.4. Mutation

Mutation is the process where the surviving population changes one or more of its attributes. This process is necessary for new information to be input to the system, otherwise it would perpetuate the genes of the starting population.

The type of mutation used, chooses individuals to mutate with a probability of 20%. Within these individuals each gene mutates with a probability of 5%, selecting a new value from within a specified range.

4.5. Common functions

The following functions that implemented to be used in both TAT and MCAT algorithms.

4.5.1. Reference frame and coordinate transformations

ECEF to ECI

This function takes a position in the ECEF reference frame and returns the position in ECI reference frame. Since the ECEF is a rotating reference frame, the ECI is an inertial one and they share the Z axis, all that is needed to transform from ECEF to ECI is a rotation of the coordinate vector around the Z axis with an angle θ such that

$$\theta = \dot{\Omega}_E.t \tag{4.15}$$

where t is the current sidereal time and Ω_E is the angular speed of the Earth around its axis ($\dot{\Omega}_E = 7.29 \times 10^{-5} rad/s$)(fig. 4.8).

$$R = \begin{bmatrix} cos(\theta) & -sin(\theta) & 0 \\ sin(\theta) & cos(\theta) & 0 \\ 0 & 0 & 1 \end{bmatrix} \tag{4.16}$$

$$pos_{ECI} = R.pos_{ECEF} \tag{4.17}$$

This transformation is only a first order approximation. It does not take into account nutation or precession movements, which would have to be accounted for in case of more precise calculations.

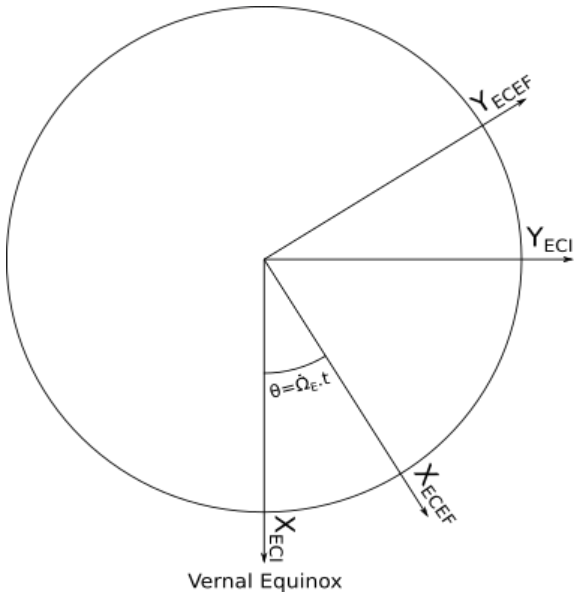

Figure 4.8: Difference between Earth centered inertial (ECI) and Earth centered Earth fixed (ECEF) reference frames.

Orbital elements to ECI

This function takes as input the Keplerian orbital elements of a satellite:

- Semimajor axis
- Eccentricity
- Inclination
- Right angle of the ascending node (RAAN)
- Argument of periapsis
- True anomaly

and returns its coordinates in the ECI reference frame as well as its velocity in this same reference frame.

The first step is to obtain the position and velocity in the perifocal reference frame

$$r_{peri} = \begin{bmatrix} a.\cos(\nu) \\ a.\sin(\nu) \\ 0 \end{bmatrix} \qquad v_{peri} = \sqrt{\frac{\mu}{a.(1+e.\cos(\nu))}} \begin{bmatrix} -\sin(\nu) \\ e+cos(\nu) \\ 0 \end{bmatrix} \tag{4.18}$$

Then, these vectors need to be rotated to the ECI reference frame using the following rotation matrix R:

$$\begin{bmatrix} \cos(\omega).\cos(\Omega) - \sin(\omega).np.\cos(i).\sin(\Omega) & -\sin(\omega).\cos(\Omega) - \cos(\omega).\cos(i).\sin(\Omega) & \sin(i).\sin(\Omega) \\ \cos(\omega).\sin(\Omega) + \sin(\omega).\cos(i).\cos(\Omega) & -\sin(\omega).\sin(\Omega) + \cos(\omega).\cos(i).\cos(\Omega) & -\sin(i).\cos(\Omega) \\ \sin(\omega).\sin(i) & \cos(\omega).\sin(i) & \cos(i) \end{bmatrix}$$

Finally, the position and velocity vectors in ECI reference frame are:

$$r_{ECI} = R.r_{peri} \qquad v_{ECI} = R.v_{peri} \tag{4.19}$$

4.5.2. Visibility determination

To determine whether a satellite has visibility of a point in space, two conditions have to be fulfilled. First, that there is a direct line of sight between the satellite and the point, meaning that the Earth does not stand between them. The second is that the point has to be within the FOV cone of the satellite's instrument.

In order to implement this, two conditions were defined. First, that the object is within the FOV cone of the satellite's instrument. The axis of this cone is defined as the pointing vector of the satellite's instrument. The generatrix of this cone is any vector with an angle of half the FOV angle of the instrument.

The second condition is a compound condition. A cone called “outer horizon (OH) cone” is defined as the cone of which the axis is the vector that points from the satellite towards the center of the Earth, and the generatrix is the vector which is tangent to the surface of the Earth. The intersection of this cone with the sphere of the Earth is a circle that lies on a plane which we will define as “OH plane”. For the second condition to be fulfilled the point has to be either between the OH plane and the satellite’s position or in case it is behind such plane, it has to be outside of the OH cone.

The second part of this condition is in order to account for objects that might be behind the OH plane which makes this algorithm different from regular visibility algorithms that only account for objects on the surface of the Earth, which is the norm of Earth observation missions.

To sum up, an object is within visibility if:

It is inside the FOV cone **and** (ahead of the OH plane **or** (behind OH plane **and** outside the OH cone))

Figure 4.9 shows a scheme indicating the FOV cone, the OH cone and the OH plane. It also shows four different cases to illustrate the visibility condition. Point **a** and **b** are ahead of the OH plane but only **b** is within the FOV cone so **a** has no visibility. Points **c** and **d** are both within the FOV cone and behind the OH plane. Only **c** is outside of the OH cone, so **d** has no visibility.

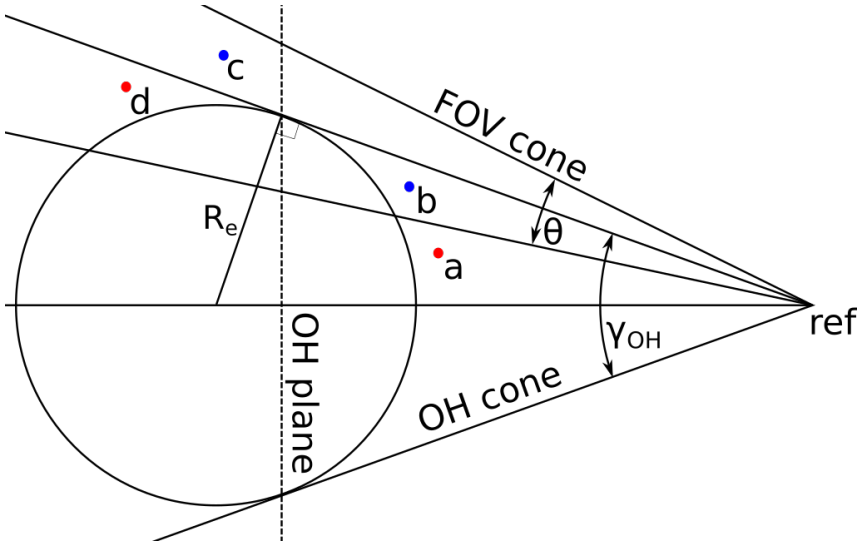

Figure 4.9: Definition of the FOV cone, the OH cone and the OH plane. The points in blue indicate points within vision from point ref whereas the two red points indicate two points not within vision.

The visibility condition is assessed by two functions:

Inside FOV

This function assesses whether a one dimensional array of points in positions **pos** are within the FOV cone from a satellite in position **ref** of which the instrument has a FOV **fov** and is pointing towards the **pointing** vector. It returns a boolean array indicating whether each point fulfills the condition.

This is done by comparing the angle γ between the **pointing** vector and the vector **r** with half the FOV angle. Vector **r** goes from the satellite to the point in space. The angle is calculated from the definition of the magnitude of the dot product between two vectors (fig. 4.10).

$$r = pos - ref \tag{4.20}$$

$$\cos(\gamma) = \frac{|r \cdot pointing|}{|r|.|pointing|} \tag{4.21}$$

$$in\_fov = \gamma < \frac{\theta}{2} \tag{4.22}$$

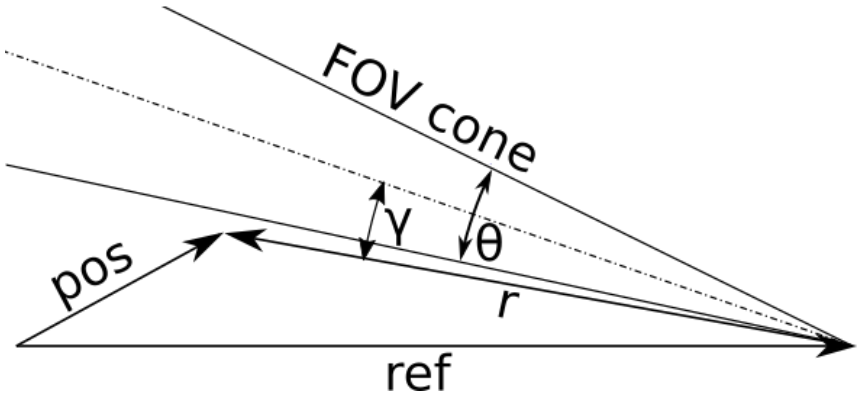

Figure 4.10: Shows the vectors **ref**, **pos** and **r** as well as the angle γ which is compared to the FOV angle θ

Within visibility

This function takes the same arguments as the previous function. It evaluates the following three conditions:

- Position respect to OH plane

  This is done by evaluating the dot product between the vector r_p with a vector $\hat{n}$ normal to the plane on the same direction as ref. Vector r_p is the one from the intersection of the plane with the ref vector ending on the position of the point. In case the dot product is positive, the point is ahead of the plane, otherwise it is behind it (fig. 4.11).

$$\hat{n} = \frac{ref}{|ref|} \tag{4.23}$$

$$|n| = \frac{{R_e}^2}{|ref|} \tag{4.24}$$

$$r_p = pos - |n|.\hat{n} \tag{4.25}$$

$$dot = \hat{n} \cdot r_p \tag{4.26}$$

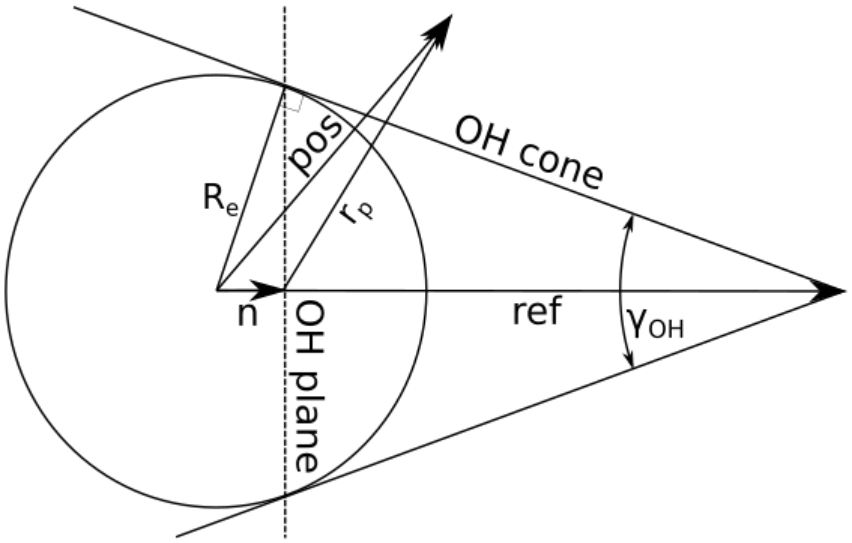

Figure 4.11: Shows the vectors ref, pos, n and r_p which are used to determine if an object located in pos is ahead or behind the OH plane.

- Position respect to FOV cone

  Evaluates whether the point is inside or outside the FOV cone using the `in_fov(...)` function.

- Position respect to OH cone

  Uses the `in_fov(...)` function to evaluate whether the point is inside or outside the OH cone by using:

  $$\gamma_{OH} = 2 * \arcsin\left(\frac{R_e}{|ref|}\right)$$

  as the fov angle and $-ref$ as the pointing vector.

Finally, the function evaluates the conditions according to the previously mentioned statement and returns a boolean array indicating whether the satellite has visibility of the points.

Two considerations to take into account are that the algorithm considers a spherical Earth and that the OH cone and plane are defined using the radius of this spherical Earth. A different radius could be used by considering an altitude at which the atmosphere becomes opaque or other visibility considerations.

4.6. Data Structures

The following are the data structures used in order to address the simulated objects.

4.6.1. Satellites

The class `satellite_circ(a,i,`Ω`,`ν`)` defines the satellite object with a circular orbit. The parameters required to initalize it are:

- Semimajor axis (a[m])
- Inclination (i[^{o}])
- Right angle of the ascending node (Ω[^{o}])
- True anomaly (ν[^{o}])

At initialization, the following parameters are defined:

- Period(`per`): $per = 2\pi\sqrt{\frac{a^3}{\mu}}$
- Position (`pos`) and velocity (`vel`) vectors: Using the `oe2eci` function
- Default nadir pointing: pointing is established as the opposite of the position vector of the satellite.

Methods

- `set_pointing(Az, El)`: Sets the satellite instrument pointing vector from arbitrary Azimuth and Elevation angles in degrees. These define the pointing vector in the satellites frame of reference.

  The X axis points away from nadir, Y axis points towards the velocity vector and Z is the one perpendicular to these two. Azimuth is relative to X axis, and elevation respect to the XY plane (fig. 4.12).

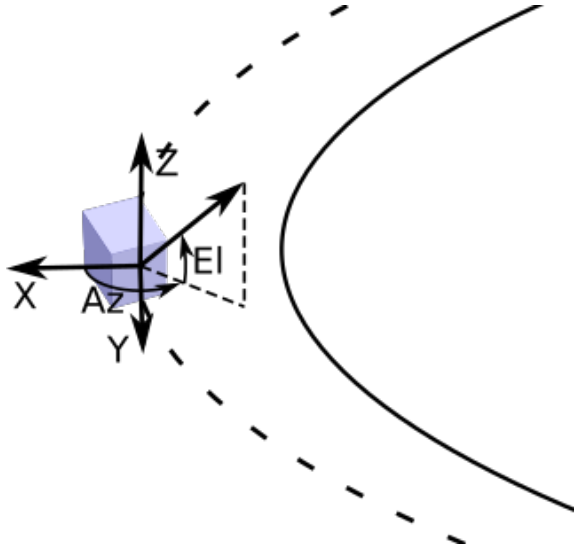

Figure 4.12: Definition of the Azimuth (Az) and Elevation (El) angles used to define the pointing attitude of the satellite.

Then, updates the satellite's pointing vector calling `update_pointing()`.

- `update_pointing()`: Sets the pointing vector in ECI coordinates from the Azimuth and Elevation angles and the position of the satellite:

$$\hat{\imath} = \frac{pos}{|pos|} \qquad \hat{\jmath} = \frac{vel}{|vel|} \qquad \hat{k} = \frac{pos \times vel}{|pos \times vel|} \tag{4.27}$$

(4.28)

$$pointing_{ECI} = cos(El)cos(Az)\hat{\imath} + cos(El)sin(Az)\hat{\jmath} + sin(El)\hat{k} \tag{4.29}$$

- `update_pos(Δt)`: Updates the satellites position and pointing by linearly advancing the true anomaly given a Δt in seconds

$$\Delta\nu = \frac{360 * \Delta t}{per}$$

$$nu_{t+1} = nu_t + \Delta\nu$$

Then, updates the satellite's pointing vector.

4.6.2. Constellation

The class `Constellation` defines the constellation object. The parameters required to initalize it are:

- Number of satellites per orbital plane (s)
- Amount of orbital planes (p)
- Separation factor (f)
- Inclination (i[^{o}])
- FOV of the satellites (fov [^{o}])
- Type of constellation (kind) Currently accepts three types of constellation:
  - Walker (kind='w')
  - Symmetric Polar (kind='sp')
  - Arbitrary orbital plane with arbitrary amount of satellites (kind='p')
- RAAN offset [^{o}]: Amount indicating how much the first orbital plane is shifted from the vernal equinox (X axis direction in the ECI frame). Default value is 0.
- ν offset [^{o}]: Amount indicating where the first satellite of the first plane is placed. Default value is 0^o, on the Equatorial plane.

At initialization the total amount of satellites (t) is calculated.

$$t = s.p$$

Depending on the `kind` parameter the intervals in orbital elements for the satellites are set differently.

- Walker

  The algorithm used is the one specified in [32].

$$PU = \frac{360}{t}$$

$$\Delta RAAN = s.PU \qquad \Delta\nu = p.PU \qquad phase = f.PU \tag{4.30}$$

- Symmetric polar

$$\Delta RAAN = \frac{180}{p} \qquad \Delta\nu = \frac{360}{s} \qquad phase = f\frac{360}{p} \qquad inc = 90 \tag{4.31}$$

- Arbitrary plane

$$p = 1 \qquad t = s \tag{4.32}$$

$$\Delta\nu = \frac{360}{s} \qquad phase = 0 \tag{4.33}$$

Then, starting from RAAN offset and the True anomaly offset, a satellite object is created in every corresponding position.

Methods

- `get_orbits()`: Returns a numpy array of size (p,360,3) with 360 cartesian coordinates of the circular orbits for each plane for graphing purposes.
- `get_positions()`: Returns a numpy array of size (t,3) with the coordinates of all the satellites.
- `get_pointing()`: Returns a numpy array of size (t,3) with the pointing vectors of all the satellites.
- `set_pointing(Az,El)`: Calls the `set_pointing(Az,El)` for every satellite setting the same pointing in the body frame to every satellite.
- `get_period()`: Returns the period of the satellites in seconds.
- `propagate_orbits(`Δ`t)`: Calls the `update_pos(`Δ`t)` method for every satellite updating their position and pointing.

4.6.3. Constellation group

The class `Constellation_Group` parses the constellation configuration json file looking for different constellation entries in the `constellation` item, which is a list. Then, it creates a `Constellation` class object for each item. This way, combinations of regular constellations or any arbitrary constellation configuration can be input by combining the constellation types previously explained.

Its methods serve as wrappers to address the methods of each `Constellation` object created.

CHAPTER 5. VERIFICATION

In order to ensure the correct functioning of the tools developed, several verification cases were studied. The extent of these cases is limited by the available data and theoretical models. The results obtained are described and discussed in this chapter.

5.1. Mass distribution

As mentioned in section 4.2.2., the sampling of distribution 4.1 is performed in a continuous manner. SWARMS uses a different approach. It generates bins of $\log(M)$ in intervals of the form $[\log_{10}(M_e), \log_{10}(M_e\delta)]$. Then, events with masses within the range of interest are generated with an uniform distribution. This method introduces error depending on the value of δ which indicates the width of the bins.

In order to benchmark the mass distribution sampling, the total mass of the generated events was compared to the total meteor mass indicated by the distribution. The distribution is a complimentary cumulative distribution function (CCDF) which relates to a cumulative distribution function through eq. 5.1, where N_{tot} is the total amount of events in the range of interest.

The derivative respect to mass of the CDF (eq. 5.2) is the event distribution function (EDF, which is not a probability density function since it indicates the amount of events for each mass). By integrating the product of the EDF times the mass of the events (M), the total meteor mass, per million km^2, per year can be calculated (eq. 5.5).

$$CCDF = N_{tot} - CDF \tag{5.1}$$

$$EDF = \frac{d(N_{tot} - CCDF)}{dm} \tag{5.2}$$

$$EDF = \begin{cases} N = -A_1 10^{B_1} M^{-A_1 - 1} & M < 2.4kg \\ N = -A_2 10^{B_2} M^{-A_2 - 1} & M > 2.4kg \end{cases} \tag{5.3}$$

$$\sum M = \int EDF \times M \tag{5.4}$$

$$\sum M = \int_{1\times10^{-4}}^{2400} -A_1 10^{B_1} M^{-A_1} + \int_{2400}^{30000} -A_2 10^{B_2} M^{-A_2} \tag{5.5}$$

$$\sum M = 388803 \frac{g}{1\times10^6 km^2 year} \tag{5.6}$$

The error from sampling is defined as the relative difference between the total normalized mass of a population of samples with the value obtained in 5.6.

In order to evaluate the error resulting from the two sampling methodologies, as well as its variability, masses were sampled with different number of samples, repeating the sampling 100 times each time. Table 5.1 and figure 5.1 show the error for each sample size as well as its standard deviation (presented as the Y axis error bars). The SWARM method was analyzed using $\log(\delta) = 0.25$.

From these results, we can conclude that for sample sizes below 1×10^6 events, the SWARMS method provides a more accurate representation, while the MCAT method does for sample size equal or above this value. On the other hand, for all sample sizes, the MCAT method results in a higher variability between each population than for SWARMS. In other words, for sample sizes above 1×10^6 the MCAT method is more accurate, and the SWARMS method is more precise.

In conclusion, using the MCAT sampling method provides a better sampling of the distribution for most cases where the sample size is big and it will be sampled several times, whereas the SWARM method might be desirable for single computations with a low amount of samples.

An analysis of the run time for each method is beyond the scope of this thesis but would be necessary for the optimization of a meteor detection design tool.

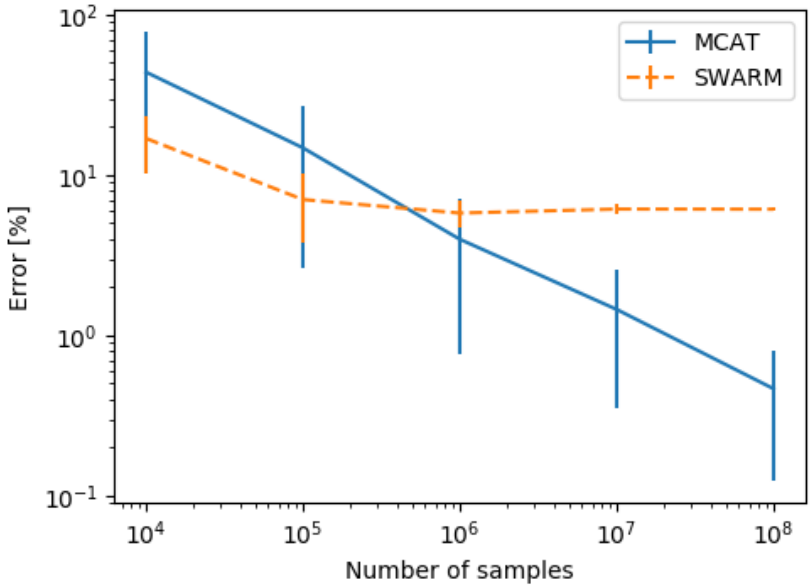

Figure 5.1: Error in total mass resulting from sampling, using two different methods used in SWARM and MCAT. The error bars indicate the standard deviation of the error.

	MCAT		SWARM	
Number of samples	**Error [%]**	**σ error [%]**	**Error [%]**	**σ error [%]**
1×10^4	43.7	33.5	16.9	6.6
1×10^5	14.7	12.1	7.0	3.2
1×10^6	4.0	3.2	5.8	1.1
1×10^7	1.4	1.1	6.1	0.4
1×10^8	0.5	0.3	6.1	0.1

Table 5.1: Results of the mass sampling benchmark, showing the error in total generated mass for different sample sizes as well as the standard deviation of the error.

5.2. Coverage surface vs altitude

The coverage area for a nadir pointing satellite with a 120º FOV instrument was calculated for different altitudes using the MCAT surface coverage tool. The results were compared to the ones obtained in [24] (fig. 5.2).

It can be seen that the shape of the curves is similar, showing two different regions: A fast growth region at the lower altitudes, where the FOV does not cover all the surface inside the OH cone (fig. 4.9) and a slower, asymptotic growth region at the higher altitudes.

The cutoff altitude between these regions can be calculated through the relationship:

$$\sin\left(\frac{\theta}{2}\right) = \frac{R_e}{R_e + alt}$$
$$alt = R_e\left(\frac{1}{\sin\left(\frac{\theta}{2}\right)} - 1\right) \tag{5.7}$$

Therefore:

$$\theta = 120^o \qquad\qquad alt = 985.6km$$

It can be seen that the MCAT calculation has the cutoff at 1000 km[1] whereas the SWARMS calculation does later.

The coverage area of a satellite with visibility not restricted to the FOV cone can be calculated through the relationship.

$$A = A_{Earth}\frac{0.5}{1 + \frac{R_e}{alt}} \tag{5.8}$$

This relationship was also plotted in figure 5.2.

It can be seen that above the cutoff value, the MCAT coverage and the geometric coverage are almost identical. The average error for MCAT above 1000 km is lower than 0.4 %.

The difference between the MCAT and SWARMS models can be explained by the difference in the point position generation, which is continuous in the former and discrete in the latter, as explained in section 4.2.2.. It can be concluded that MCAT calculates coverage surface better than SWARMS and to a very good level of accuracy.

[1] Discretization of MCAT X axis of 100km

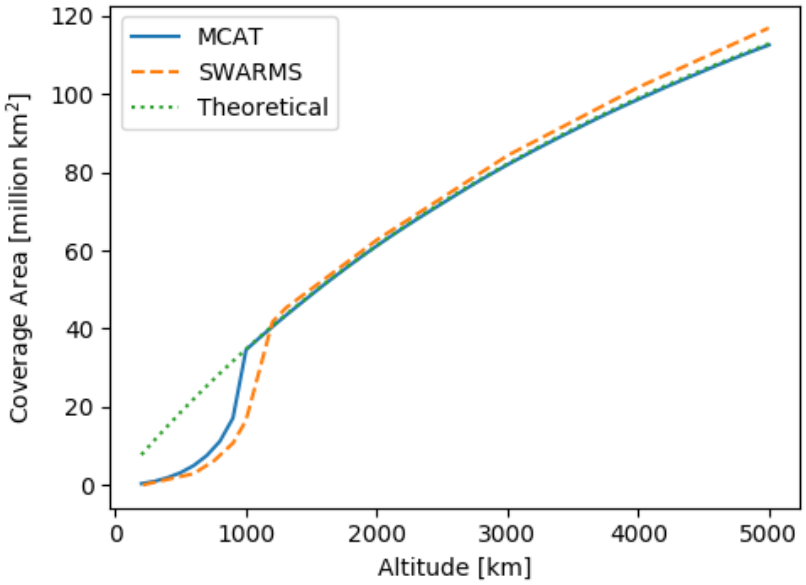

Figure 5.2: Coverage area on the Earth's surface from a nadir pointing satellite with an instrument with a FOV of 120°, as calculated with the SWARM model, with the MCAT surface coverage tool and using a geometric relationship.

5.3. Coverage vs tilt angle

One of the cases studied in [24] is the JEM-EUSO experiment onboard the ISS [33]. This experiment consists of a camera with a FOV angle of 60°. Its objective is to document luminous events in the upper atmosphere, particularly fluorescence produced by cosmic rays. Its orbit altitude is 400 km.

The Earth coverage area of a camera of these characteristics was calculated for different tilt (respect to nadir) angles and compared with the data from SWARMS.

As can be seen in figure 5.3, MCAT shows a higher coverage area for lower tilt angles, coinciding with the results obtained in the previous section. MCAT gives the maximum value around 60° whereas SWARM does around 70°.

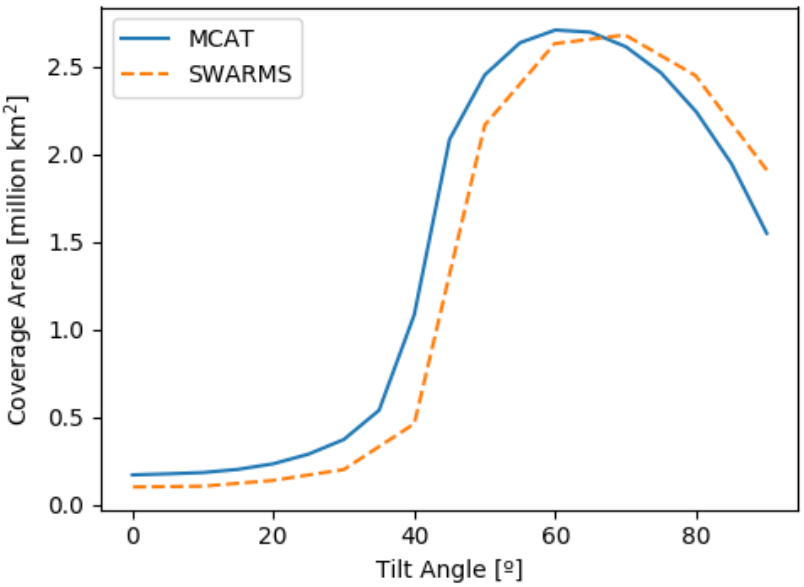

Figure 5.3: Coverage area on the Earth's surface from a tilted satellite. Calculated with the SWARM model and with the MCAT surface coverage tool.

5.4. Detection rate vs altitude

The meteor detection rate for a nadir pointing satellite with a 120^o FOV instrument was calculated for different altitudes using MCAT but without the diurnal variation weight scheme. The results were compared to the ones obtained in [24].

As can be seen in figure 5.4, the results obtained with MCAT are within the same range as SWARMS, but slightly higher above 1500 km. The variability in detection rates, generated by the random nature of the algorithm can be observed. This could be of course solved by increasing the amount of particles used, and therefore computational requirements.

In order to observe the effect of events seen through the atmosphere, a modified version of MCAT that does not detect these events was evaluated. Furthermore, a version of MCAT with mass generation using the SWARMS algorithm was used. No significant difference was found.

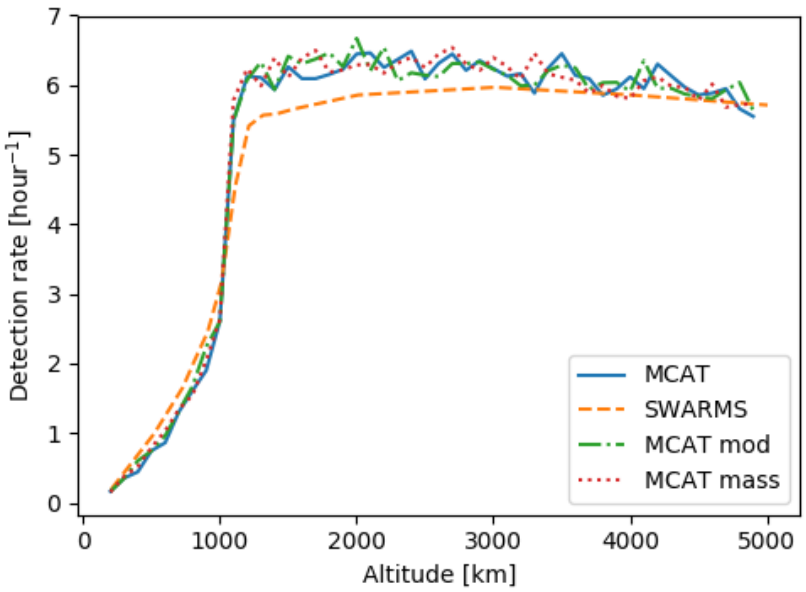

Figure 5.4: Hourly detection rate of a nadir pointing satellite with an instrument with a FOV of 120^{o} respect to altitude. Calculated using SWARMS, MCAT, a modified version of MCAT that does not consider events detected through the atmosphere and a modified version that generates mass using SWARMS.

5.5. Detection rate vs tilt angle

The meteor detection rate of a satellite as described in section 5.3. was calculated for different tilt (respect to nadir) angles and compared with the data from SWARMS.

It can be seen in Figure 5.5 that the results obtained with MCAT have the same shape and are within the same order of magnitude as SWARM but with a higher detection rate at higher tilt angles. This is probably related to the higher covered surface at 400 km compared to SWARMS.

A modified version of MCAT which does not consider events that can be detected through the atmosphere was also ran and the results were found to be almost identical to the standard one.

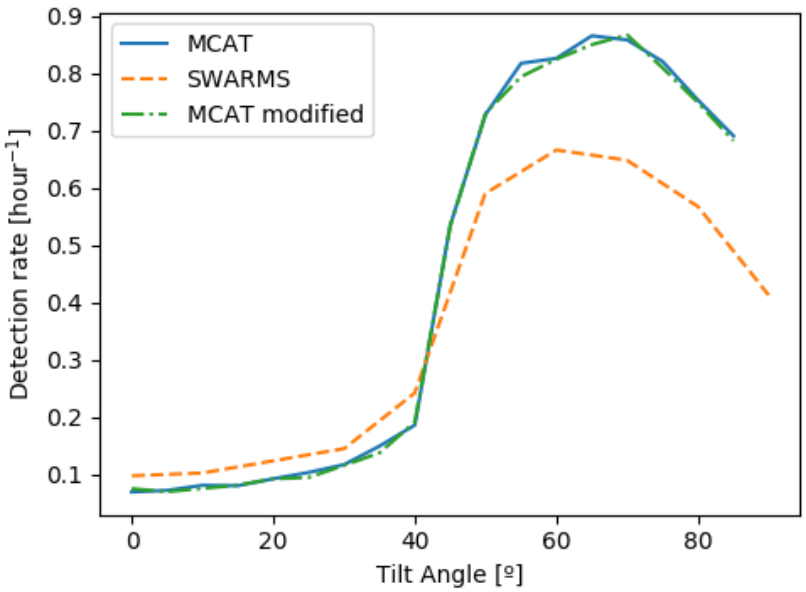

Figure 5.5: Hourly meteor detection rate for a camera with a FOV of 60^{o}. Calculated using SWARMS, MCAT and a modified version of MCAT that does not consider events detected through the atmosphere.

5.6. Comments on verification

The verifications here presented show that MCAT performs just as well, and in some aspects, with more accuracy than the SWARMS code. The results regarding detection rates do not coincide exactly, but do with a high level of agreement. Taking into account the high sensitivity of detection rates with meteor property distributions (which is also noted in [24]), the benchmarks show that the code is good enough to produce comparable results to other works and to serve as a qualitative analysis tool for mission design.

Undoubtedly, the results obtained will have to be validated and adjusted once experimental data from a real mission is available in order to be able to develop quantitative analysis tools.

CHAPTER 6. USE CASES

As mentioned before, the focus of this thesis is on the development of tools to study the performance of orbital observatories of meteors and atmospheric reentries. Instead of looking for a specific solution or result, this section presents some use cases, which showcase the use of the tools developed to find close to optimal parameters to proposed mission geometries.

6.1. Meteor detection: Chaser configuration

This configuration proposal is a minimalistic constellation design consisting of two satellites in the same Sun synchronous orbit. It seeks to maximize the double detection rate by having one satellite "chasing" the other at a certain distance and have both satellites pointing at the same region of the atmosphere.

Configuration parameters

Fixed

The fixed parameters, those that do not change from solution to solution, are presented in table 6.1.

Parameter	Value
FOV [^{o}]	84
Orbital planes	1
Number of satellites	2

Table 6.1: Fixed parameters for the chaser configuration optimization.

The FOV chosen is that of the LEICA camera proposed in the latest iteration of the METEORIX project [23].

Variable

The variable parameters, those bound to be optimized, are presented in table 6.2.

Parameter	Minimum	Maximum
Altitude [km]	200	2000
RAAN [^{o}]	0	360
Pointing azimuth [^{o}]	135	225
Pointing elevation [^{o}]	0	45
ν separation [^{o}]	10	45

Table 6.2: Variable parameters for the chaser configuration optimization.

The angular separation, or difference in true anomaly of each satellite, has a lower bound of 10^o. If it did not, the optimal solution would tend to having no separation, meaning both satellites are in the same point in space. Such configuration would result in both satellites detecting the same events, but with a very low or null convergence angle (concept explained in section 7.1.). In order to obtain a configuration which yields observations with a good convergence angle, and also to aid visualization, this parameter was chosen this way.

Sun synchronous orbits are those in which the precession of the orbit due to the perturbations caused by the non-sphericity of Earth is synchronized with the rotation of the Earth around the Sun. To our ends, it means that the orbit will remain the same with respect to the night side of Earth with almost no need for station keeping. This would result in a lighter, and therefore cheaper mission than one with inclination not related to the altitude.

The inclination (i) was thus restricted to:

$$\cos(i) = -\left(\frac{R_{Earth} + altitude}{12352km}\right)^{3.5} \tag{6.1}$$

Results

The case was optimized using 100 generations of 16 individuals.

Figure 6.1 shows the evolution of the minimum, maximum and average fitness scores for each generation. It can be seen that the average fitness of the population, and the fitness of the fittest individual, increases over the generations, replicating the effects of an evolutionary process. Around generation 40 there is an upwards step in fitness, which might be the result of a particularly well fitted mutated individual, or a crossover which resulted in different parameters working in a synergetic way.

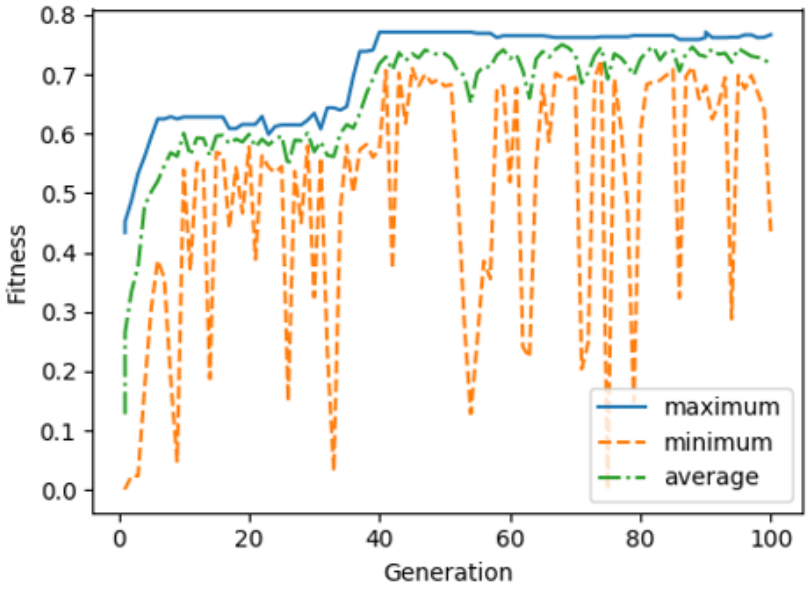

Figure 6.1: Average, minimum and maximum fitness scores for each generation in the genetic optimization for a Sun synchronous “chaser” constellation.

The fittest solution found has a fitness score of **0.71**, meaning that this configuration would result in a hourly double detection rate of **1.42**. The solution's parameters can be found in table 6.3.

Parameter	**Satellite 1**	**Satellite 2**
Altitude [km]	1958	
Inclination [^{o}]	104.77	
Pointing azimuth [^{o}]	144	181
Pointing elevation[^{o}]	28	15
RAAN [^{o}]	344	
ν separation [^{o}]	19	

Table 6.3: Optimized parameters for the Sun synchronous chaser cofiguration.

For comparison purposes, a population of 1600 random individuals was drafted. The fittest individual's score was **0.51**, corresponding to an hourly double detection rate of **1.02**. This shows that in this case the genetic algorithm found a better solution than the one obtained from a group of random individuals that take the same or more analysis time.[1]

The solution obtained is a very sensible one. The satellites are overlapping their observation footprints and they are pointing towards the night side of Earth. Furthermore, the constellations RAAN is close to the dusk-dawn line but slightly shifted in RAAN so that it has a better visibility of the dawn side of Earth which has a higher meteor flux. Figure 6.2 shows a sequence of the satellites going around Earth showing the overlapping observation footprints.

From an engineering point of view, even though the altitude obtained gives a higher double detection rate, it might cause trouble on a systems level. This altitude is within a region known as the "inner Van Allen radiation belt", with a high density of energetic charged particles. This high radiation field could potentially damage or produce malfunctions in the spacecraft's systems, degrading or terminating the mission. A solution to this would be to accept the shorter lifetime of the mission, use radiation hardened components, which are more expensive, or limit the altitude to a lower region of space.

On the other hand, the RAAN, combined with the Sun synchronous characteristic, is highly beneficial since both spacecraft would be constantly, or almost constantly facing the Sun. This means that eclipses would be very short or inexistent. Therefore, the batteries for the power subsystem would have to be smaller and subject to a lower workload than those for a mission constantly having long eclipse times.

This kind of mission could be easily launched with a single rocket carrying both satellites. Maybe even the SpaceLabs electron rocket in case the satellites are cubesats and an altitude below 700 km is chosen; this rocket is designed to launch multiple payloads into Sun synchronous orbits [34].

[1] At each generation, only the new individuals' fitness is analyzed.

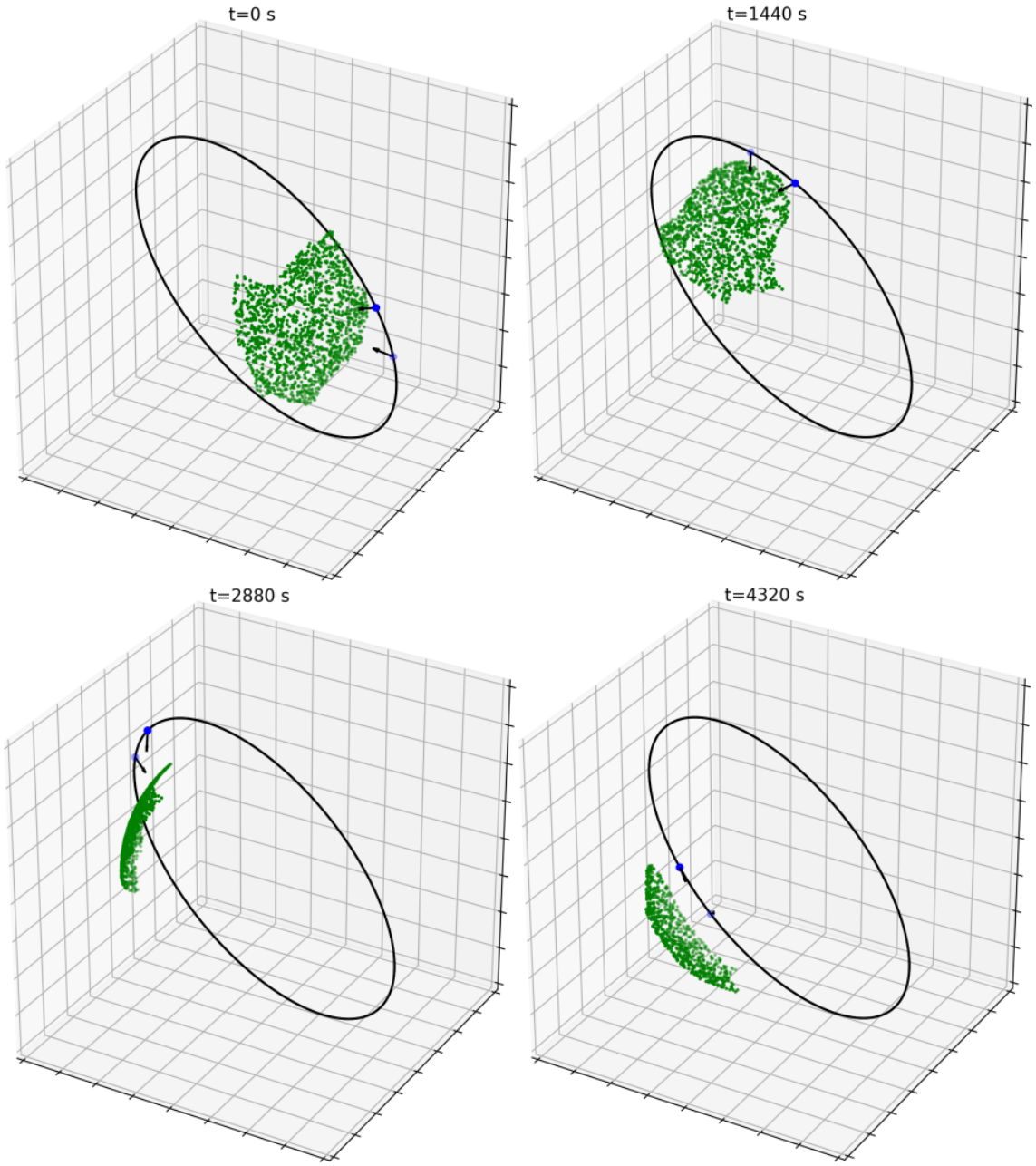

Figure 6.2: Image sequence showing the optimized chaser configuration orbiting Earth, as well as the satellites' observation footprints.

6.2. Object tracking: 3-plane Walker delta constellation

In this use case, the constellation consists of a 3-plane Walker delta constellation, leaving the amount of satellites per plane as one of the parameters to optimize. The target track used is an arbitrary parabolic track corresponding to a launch vehicle with a ballistic trajectory.

Configuration parameters

Fixed

The fixed parameters are presented in table 6.4.

Parameter	Value
FOV [^{o}]	60
Orbital planes	3

Table 6.4: Fixed parameters for the 3-plane Walker delta constellation optimization.

As the algorithm evaluates several different starting points in time regarding ECEF position respect to ECI, the RAAN was fixed to 0^o, but any value would yield the same results.

Variable

The variable parameters are presented in table 6.5.

Parameter	Minimum	Maximum
Altitude [km]	200	2000
Satellites per plane	1	10
Pointing azimuth [^{o}]	120	240
Pointing elevation [^{o}]	0	60
Inclination [^{o}]	0	90
f	0	2

Table 6.5: Variable parameters for the 3-plane Walker delta constellation optimization.

Results

The case was optimized using 30 generations of 16 individuals.

The optimized constellation configuration corresponds to a 49^o:27/3/0 Walker delta configuration. The optimized parameters can be found in table 6.6.

Its score is **0.02037**, meaning that, in average, the constellation will be able to track the object with two or more satellites for **55%** of the track's time.

Parameter	Value
Satellites per plane	9
Altitude [km]	1517
Inclination [^{o}]	49
Pointing azimuth [^{o}]	120
Pointing elevation[^{o}]	24
f	0

Table 6.6: Optimized parameters for the 3-plane Walker delta cofiguration.

This particular constellation configuration uses a very high amount of satellites (comparable to the GPS or Galileo networks) and would require at least 3 different launches in the case the satellites were cubesats.

Taking into account the same considerations as in the previous examples, the altitude might have to be modified for the satellites to be in a lower radiation area and avoid having to use radiation resistant components.

Differently to the results in the previous example, the batteries would have to be dimensioned in the usual way, accounting for one eclipse for every orbital period.

Figure 6.3 shows the output of the analysis for this particular configuration showing the average amount of satellites tracking the object.

Figure 6.4 shows an image sequence showing the constellation tracking the launch vehicle at different points in time.

For comparison purposes, a population of 480 (30x16) random individuals was drafted. The fittest individual's score was **0.03039**. This score is higher than the one of the solution found.

Being a stochastic process, the sampling of the solution space, there is a chance of finding an optimum or close to optimum solution by choosing random individuals. The idea of the optimization algorithm is to obtain better solutions with less computations. In this case this is not happening, but would probably for a higher number of generations, with larger populations or more advanced algorithms.

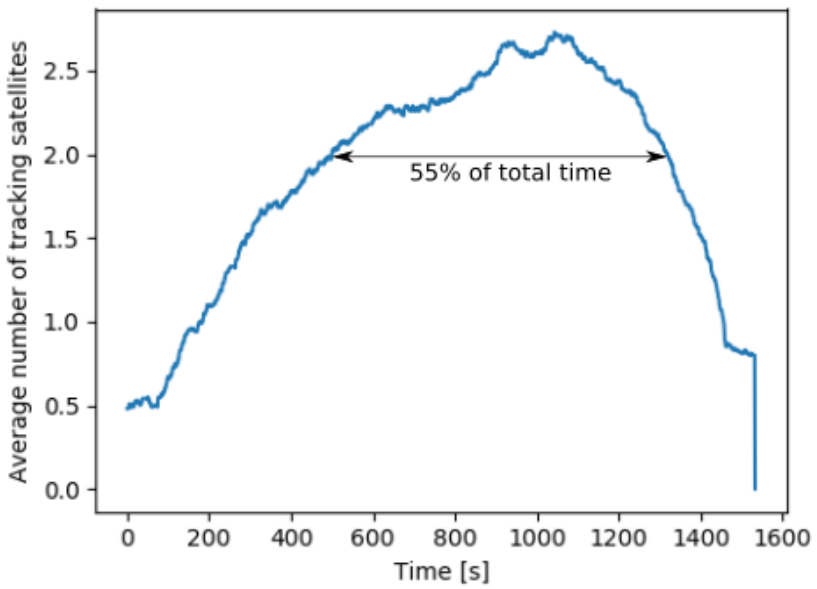

Figure 6.3: Average amount of tracking satellites of a 3-plane Walker delta constellation for an object with a parabolic trajectory. The time where the launch vehicle is being tracked by more than 2 satellites is indicated.

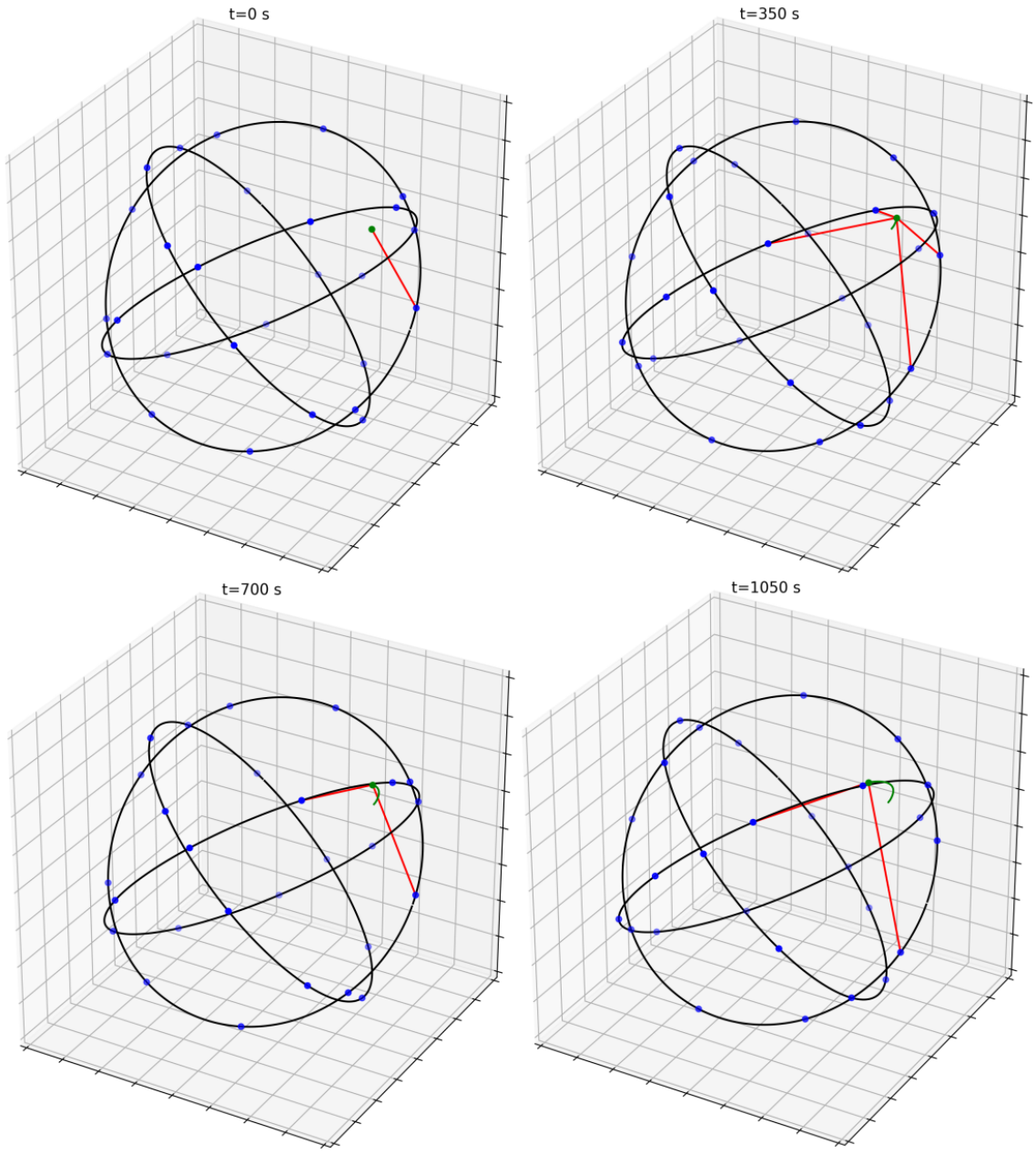

Figure 6.4: Image sequence showing the optimized 3-plane Walker delta constellation satellites (blue) tracking the launch vehicle (green) at different points in time. A red line is drawn when a satellite is tracking the vehicle.

CHAPTER 7. CONCLUSIONS

Even though significant efforts and advances have been done in the last decades to improve our understanding of meteor science, space debris and vehicle reentry, there still remains an almost untapped niche, which is orbital observation of these phenomena.

In this thesis, the need for and advantages for a satellite constellation mission for meteor detection and object reentry observation were explored and used as a motivation driver. With these considerations in mind, sets of objectives and requirements appropriate for this kind of missions were laid down.

A suite of tools for constellation performance analysis was developed in order to aid in feasibility studies and early stage design of these constellations. The first being a tool that estimates the average hourly single and multiple meteor detection rates of a constellation. The other, for evaluating how well the constellation can track a longer event such as the reentry of a spacecraft.

A simple genetic optimization algorithm was implemented in order to demonstrate how the combination of these tools could be used to obtain optimized constellation designs with a fairly big variable space.

Verifications were made by contrasting the results obtained with the tools with those presented for one of the state of the art publications on orbital meteor detection [24]. The tools proved to work just as well, or in some cases better, than the work used for comparison. Further verification and validation remains to be done for the functions for which no adequate comparison was available.

Finally, two use cases were presented, exploring the use of the tools in combination to design different constellation architectures.

Hopefully, the tools presented here will serve as stepping stones for future mission designs, and help broaden humanity's understanding of space technology and the cosmos.

7.1. Future work

The following are some items which the author considers as the next steps for a future iteration of meteor detection and object reentry observation constellation analysis tools.

- Tracking quality using convergence angle

  Convergence angle is the angle that is formed between two observations of the same event. The precision with which the position of an event is calculated is proportional to the cosine of this angle. This concept in global navigation satellite services is known as “dilution of precision”.

  In order to asses the quality of a multiple observation, the convergence angle for each observation would have to be calculated. A description of different algorithms can be found in [35].

- Modeling of meteors as line segments with variable luminosity

  In this thesis, meteors were modeled as instantaneous point sources of an averaged luminous intensity. The next step would be to consider meteors as line segments with a starting point, an end point, a duration and variable luminous intensity. The light curves could be obtained using the “Script for analysis of meteor trajectories” mentioned in [24], from meteor observation sources such as [26].

- Elliptical and perturbed orbits

  In order to implement more complex constellations such as the ones described in section 1.5., elliptical orbits would have to be implemented. This would imply, among other simpler calculations, to solve Kepler’s equation for each satellite at each time step. This equation is transcendental and has to be solved using numeric metods. A better insight can be found in [36]. A further step would be to implement perturbations to the orbits to account for changes such as precession of the nodes or regression of the absides.

- Algorithm optimization

  Even though the algorithm performs well, it is computationally intensive, requiring around 6 hours for the optimizations in chapter 6 and the amount of meteors generated per time step being limited by memory. There is plenty of room for optimizations in the code to make it faster and more efficient.

ACKNOWLEDGEMENTS

I would like to thank, first and foremost, to my family who is always there for me.

During the course of this thesis, I was in contact with people related to the SWARMS paper, who are also developing the FRIPON and METEORIX projects. Namely Jérémie Vaubaillon, Nicolas Rambaux and Lionel Lacasagne. They were kind enough to share with me their own tools and were eager to help me out by answering questions as well as discussion on research goals. Their help proved to be very constructive and motivating and I am very grateful for it.

A big thank you to my Director at Airbus Andreas Stock for guiding me through this work, and to al the BG8 squad for making this time so much nicer.

Finally, I would like to also thank Nico, who will never get rid of my questions, and Clara, for helping me in so many other ways.

BIBLIOGRAPHY

[1] Z. Ek and R. L. Hawkes, *W. graham elford*. 1998. xiii, 2, 4, 26

[2] J. Borovička, "Two components in meteor spectra," *Planetary and Space Science*, vol. 42, no. 2, pp. 145–150, 1994. 4

[3] V. Vojáček, J. Borovička, P. Koten, P. Spurný, and R. Štork, "Catalogue of representative meteor spectra," *Astronomy & Astrophysics*, vol. 580, p. A67, aug 2015. xiii, 5

[4] P. Jenniskens, E. Tedesco, J. Murthy, C. O. Laux, and S. Price, "Spaceborne ultraviolet 251-384 nm spectroscopy of a meteor during the 1997 Leonid shower," *Meteoritics and Planetary Science*, 2002. xiii, 5, 14

[5] S. Pizzarello and E. Shock, "The organic composition of carbonaceous meteorites: the evolutionary story ahead of biochemistry.," *Cold Spring Harbor perspectives in biology*, vol. 2, no. 3, pp. 1–19, 2010. 6

[6] P. D. Maley, "Earth based observations of the STS-11 space shuttle mission on orbit and during reentry," *Acta Astronautica*, 1985. 7

[7] ESA, "How many space debris objects are currently in orbit?," 2013. 7

[8] D. Lear, J. Hyde, E. L. Christiansen, J. Herrin, and F. Lyons, "STS-118 Radiator Impact Damage," *NASA Report*, no. August 2007, pp. 10–13, 2007. xiii, 7

[9] F. Zander, S. Lemmens, H. Krag, H. Enthalpy, F. Diagnostics, and S. D. Office, "Airborne Observations of Re-Entry Break-Up : Results and Prospects," no. April, pp. 18–21, 2017. 8

[10] T. J. Horvath, M. F. Cagle, J. H. Grinstead, and D. M. Gibson, "Remote observations of reentering spacecraft including the space shuttle orbiter," *IEEE Aerospace Conference Proceedings*, 2013. xiii, 8

[11] T. Horvath, D. Tomek, S. Splinter, J. Zalameda, P. Krasa, R. Schwartz, D. Gibson, A. Tietjen, and K. Berger, "The Hythirm Project: Flight Thermography of the Space Shuttle During Hypersonic Re-Entry," *48th AIAA Aerospace Sciences Meeting Including the New Horizons Forum and Aerospace Exposition*, pp. 4–7, 2010. xiii, 8

[12] S. Clark, "Managers confident ahead of critical launch for Galileo navigation system – Spaceflight Now." xiii, 10

[13] J. R. Wertz and W. Larson, *SMAD - Space Mission Analysis and Design*. 1999. 10

[14] D. Mortari, "Flower constellations as rigid objects in space," *European Space Agency, (Special Publication) ESA SP*, vol. 633 SP, pp. 7–22, 2006. 10

[15] T. W. Beech, S. Cornara, M. B. Mora, and S. A. Gmv, "A study of three satellite constellation design algorithms," *International Symposium on Space Flight Dynamics*, 1999. 11

[16] G. H. Parker, *Navigation constellation design using a multi-objective genetic algorithm*. PhD thesis, Air Force Air University, Wright-Patterson Air Force Base, Ohio, 2006. 11

[17] T. Savitri, Y. Kim, S. Jo, and H. Bang, "Satellite Constellation Orbit Design Optimization with Combined Genetic Algorithm and Semianalytical Approach," *International Journal of Aerospace Engineering*, vol. 2017, pp. 1–17, may 2017. 11

[18] Herbert J. Kramer, "MSX (Midcourse Space Experiment)." xiii, 13, 14

[19] P. Brown, R. E. Spalding, D. O. ReVelle, E. Tagliaferri, and S. P. Worden, "The flux of small near-earth objects colliding with the earth," *Nature*, vol. 420, no. 6913, pp. 294–296, 2002. 14

[20] J. F. Rapp and D. S. Draper, "45th Lunar and Planetary Science Conference (2014) 1527.pdf," pp. 11–12, 2014. 15

[21] NASA, "A space based view of meteor showers." xiii, 15

[22] M. Ortega, V. De Seijas, and O. Varela De Seijas M, "Design of a 3U cubesat for metor detection and characterizaton.," pp. 26–30, 2016. 15

[23] N. Rambaux, P. Keckhut, A. Hauchecorne, D. Galayko, G. Guignan, J. Vaubaillon, L. Lacassagne, M. Birlan, P. Boisse, M. Capderou, F. Colas, F. Deshours, J.-F. Mariscal, B. Zanda, G. Augarde, S. Barnier, S. Ben Kemmoum, A. Bigot, A. Chu, D. Portela Moreira, J. Raffard, M. Lumbroso, C. Tob, A. Hennequin, Y. Fargeix, T. Romera, T. Koehler, J. L. Rault, and A. Chantal Levasseur-Regourd, "Meteorix: a cubesat mission dedicated to the detection of meteors," *42nd COSPAR Scientific Assembly. Held 14-22 July 2018, in Pasadena, California, USA, Abstract id. B0.2-23-18.*, vol. 42, 2018. xiii, 16, 51

[24] A. Bouquet, D. Baratoux, J. Vaubaillon, M. I. Gritsevich, D. Mimoun, O. Mousis, and S. Bouley, "Simulation of the capabilities of an orbiter for monitoring the entry of interplanetary matter into the terrestrial atmosphere," *Planetary and Space Science*, vol. 103, pp. 238–249, 2014. 23, 25, 27, 28, 45, 46, 47, 49, 59, 60

[25] H.-G. Muller, "Change-Points in Nonparametric Regression Analysis," *The Annals of Statistics*, vol. 20, no. 2, pp. 737–761, 1992. 24

[26] I. Halliday, A. A. Griffin, and A. T. Blackwell, "Detailed data for 259 fireballs from the Canadian camera network and inferences concerning the influx of large meteoroids," *Meteoritics and Planetary Science*, vol. 31, no. 2, pp. 185–217, 1996. 25, 27, 30, 60

[27] S. M. Hunt, M. Oppenheim, S. Close, P. G. Brown, F. McKeen, and M. Minardi, "Determination of the meteoroid velocity distribution at the Earth using high-gain radar," *Icarus*, vol. 168, no. 1, pp. 34–42, 2004. 26

[28] C. Szasz, J. Kero, A. Pellinen-Wannberg, J. D. Mathews, J. D. Mathews, and N. J. Mitchell, "Latitudinal Variations of Diurnal Meteor Rates," 2006. xiv, 28, 69

[29] F. A. Fortin, D. Rainville, M. A. G. Gardner, M. Parizeau, and C. Gagné, "DEAP: Evolutionary Algorithms Made Easy," *Journal of Machine Learning Research*, vol. 13, pp. 2171–2175, 2012. 31

[30] “DEAP Github repository - https://github.com/DEAP/deap.” 31

[31] D. G. Trist and T. P. Kenakin, “Editors in Chief Overview,” *Current Opinion in Pharmacology*, vol. 35, pp. iv–v, 2017. 31

[32] J. R. Wertz, *Mission Geometry; Orbit and Constellation Design and Management*. Soringer, 1 ed. 40

[33] T. Ebisuzaki, G. Medina-Tanco, and A. Santangelo, “The JEM-EUSO mission,” *Advances in Space Research*, vol. 53, pp. 1499–1505, may 2014. 46

[34] Rocket Lab, “Payload User’s Guide,” no. August, 2018. 53

[35] J. Borovička, *The comparison of two methods of determining meteor trajectories from photographs*, vol. 41. EDP Sciences [etc.], 1990. 60

[36] R. R. Bate, D. D. Mueller, and J. E. White, *Fundamentals of Astrodynamics*. New York: Dover Publications, Inc., 1st ed., 1971. 60

APPENDICES

APPENDIX A. DATA USED FOR DIURNAL FLUX VARIATION WEIGHT SCHEME

The data used to fit the diurnal flux variation weight function was extracted from the graphs in figure A.1 from [28]. The average for every location and season and for each hour was obtained. It is presented in table A.

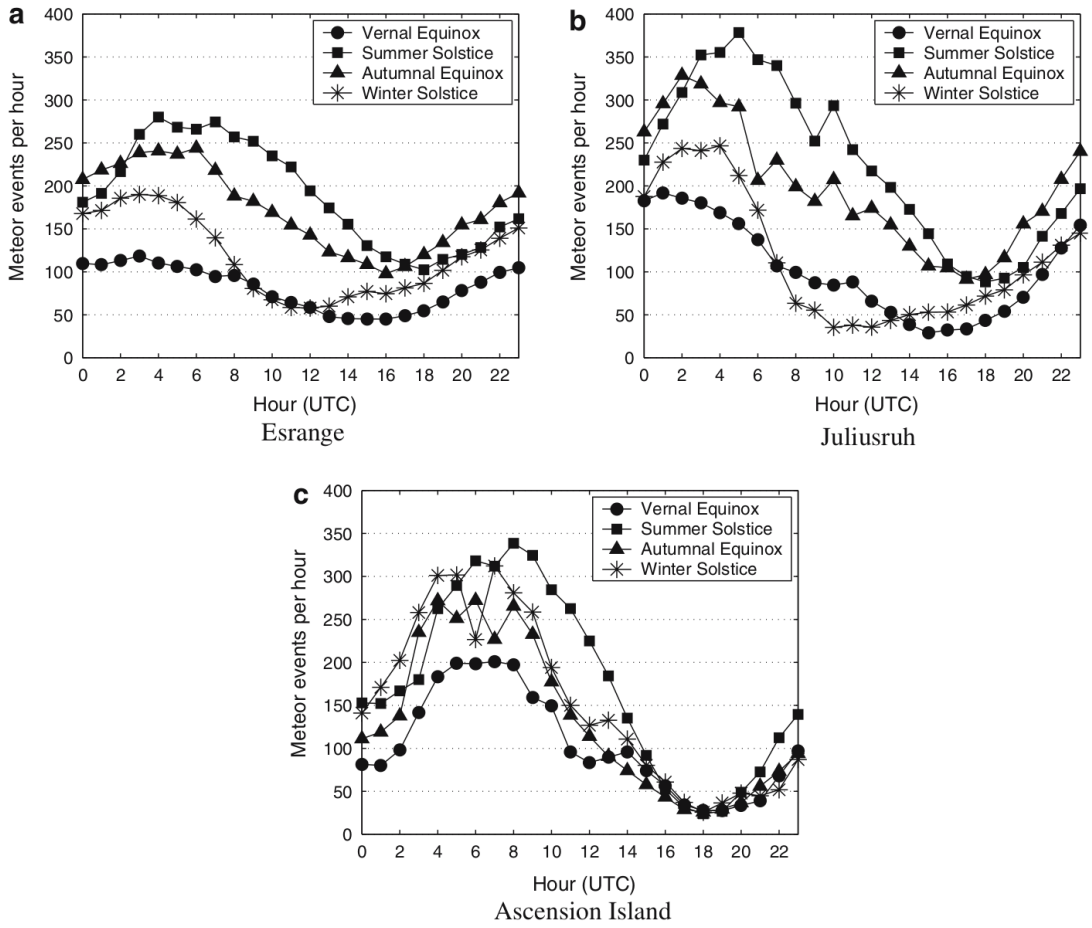

Figure A.1: Graphs of the data used to fit the diurnal flux variation weight function [28].

Hour	Average hourly meteor flux
0	168.16
1	183.40
2	201.43
3	226.24
4	242.65
5	239.74
6	221.67
7	214.02
8	199.68
9	179.78
10	164.02
11	140.59
12	124.59
13	113.04
14	100.27
15	83.84
16	70.82
17	63.87
18	64.31
19	73.85
20	88.90
21	103.52
22	126.47
23	148.20

Table A.1: Averaged diurnal flux variation data used for the weight function.